

Nonperturbative Lattice Simulation of High Multiplicity Cross Section Bound in ϕ_3^4 on Beowulf Supercomputer

Yeo-Yie Charng

*Department of Physics
University of Pittsburgh
Pittsburgh, PA 15260*

Abstract

In this thesis, we have investigated the possibility of large cross sections at large multiplicity in weakly coupled three dimensional ϕ^4 theory using Monte Carlo Simulation methods. We have built a Beowulf Supercomputer for this purpose. We use spectral function sum rules to derive a bound on the total cross section where the quantity determining the bound can be measured by Monte Carlo simulation in Euclidean space. We determine the critical threshold energy for large high multiplicity cross section according to the analysis of M.B. Volosion and E.N. Argyres, R.M.P. Kleiss, and C.G. Papadopoulos. We compare the simulation results with the perturbation results and see no evidence for large cross section in the range where tree diagram estimates suggest they should exist.

Table of Contents

1	Introduction	2
2	Beowulf Parallel Supercomputer	4
2.1	The Beowulf Project History	4
2.2	Definition of the Beowulf Supercomputer	4
2.3	Architecture and System Design	5
2.3.1	Hardware Configuration	7
2.3.2	Software Configuration	8
2.4	Performance and Benchmark	8
3	The Cross Section and Bound	11
3.1	Definition of the inclusive cross section	11
3.2	Spectral Representation and Sum Rules	13
3.3	Spectral Representation of G^{-1}	14
3.4	Upper Bound of Inclusive Cross Section	17
4	Critical Energy and the Relation to Euclidean Momentum	18
4.1	Amplitude for $f\bar{f} \rightarrow n\phi$	18
4.2	The Phase Space	21
4.3	The Critical Energy and The relation to Lattice Momentum	24
5	Lattice Simulation	27
5.1	Monte Carlo Simulation	27
5.2	Cluster Update Algorithm	30

5.3	Continuum Limit	31
5.4	The Simulation Methods	37
5.5	Verify the Ising limit of the Simulation	38
6	The Perturbation Calculation	40
6.1	ϕ_3^4 model and renormalization	40
6.2	One-Loop calculation for $\frac{\langle\phi_0\rangle}{\sqrt{m'}}$	43
6.3	The calculation for $\frac{1}{Z'}$ to $O(\lambda^2)$	44
7	Analysis and Results	49
7.1	The Results From the Simulation	49
7.2	Discussion and the Conclusion	54
A	Multiple zeros case for the function $g^{-1}(z)$	56

List of Figures

2.1	The architecture of the Beowulf Supercomputer	6
2.2	The HPL Benchmark shows the speed scales up linearly.	10
3.1	The amplitude $A(n; E)$ for $\phi \rightarrow n\phi$	12
3.2	The amplitude for $f\bar{f} \rightarrow n\phi$, to lowest order in g_y	12
3.3	The pole and structure for $g(x)$	15
4.1	Diagrammatic structure of the recursion relation for ϕ^4 interactions in symmetry case	19
4.2	Diagrammatic structure of the recursion relation for mixed ϕ^4 and ϕ^3 interaction	20
5.1	Result of Monte Carlo evaluation of $G_0^{-1}(\vec{p})$ plotted against exact analytic massless $G_0^{-1}(\vec{p}) = 4 \sum_{\mu} \sin^2(p_{\mu})^{-1} \equiv \vec{p}^2$ at 32^3 lattice. Error bars on Monte Carlo results are too small to show up on this plot. . .	29
5.2	The autocorrelation for the $\langle \phi \rangle$ with and without the cluster update algorithm. The e^{-1} point for the one without the cluster update algorithm is at about 400(top). The autocorrelation length for the one with cluster update algorithm is about 2 only(bottom).	32
5.3	The scaling of the continue limit. When we halve the lattice constant, $a \rightarrow a/2$, the correlation length, ξ_L , will be doubled $\xi_L \rightarrow 2\xi_L$	34
5.4	The two parameters (λ, a) phase diagram for different limits	35
5.5	The two parameters (λ, a) phase diagram. The diagram shows the statistical mechanical approach for both $d < 4$ and $d > 4$. The dashed arrow shows the field theory approach.	35

5.6	The phase diagram for the three-dimensional, single component scalar ϕ^4 theory. The solid line separates the symmetric phase from the broken symmetry phase. The dash-dot lines represent lines of constant physics in the symmetry phase, and the dashed lines are lines of constant physics in the broken phase. The origin is the Gaussian limit and does not imply a trivial field theory for $d < 4$	36
6.1	The one-loop tadpole diagram and the counter term.	42
6.2	The one-loop self energy diagrams.	42
6.3	The one-loop Feynman diagrams for $n = 2(\mathcal{G}_3^{\frac{3}{2}})$	45
6.4	The tree diagrams for $n = 3(\mathcal{G}_2^2)$	45
7.1	Continuum limit for the $\frac{\lambda}{m'}$. The plot shows the insensitivity of lattice size for $\frac{\lambda}{m'}$	51
7.2	Continuum limit for the $\frac{1}{Z'}$. The plot shows the insensitivity of lattice size for $\frac{1}{Z'}$	52
7.3	Continuum limit for the $\frac{\langle\phi_0\rangle}{\sqrt{m'}}$. The plot shows the insensitivity of lattice size for $\frac{\langle\phi_0\rangle}{\sqrt{m'}}$	53
A.1	The function of $g(z)$ with one zero.	57

List of Tables

2.1	NAS Benchmark	9
2.2	HPL Benchmark	9
5.1	Comparison of the values of the dynamic exponent z for different algorithms for Ising model in various dimensions[28].	30
5.2	The Monte Carlo simulation of $32^3 \phi_3^4$ theory at Ising limit($\lambda \rightarrow \infty$). The table shows the critical temperature β_c at different λ values.	39
7.1	The results of our simulations on different size lattices(N). The output correlation length $\xi'_L = 1/m'_L$, the dimensionless ratios λ/m' , and $1/Z'$ are given.	50
7.2	The finite size effect with fixed input parameters $\mu_{0L}^2 = 0.078$, $\lambda_L = 0.1$	50
7.3	The finite size effect with fixed input parameters $\mu_{0L}^2 = 0.0384$, $\lambda_L = 0.05$	50
7.4	The finite size effect with fixed input parameters $\mu_{0L}^2 = 0.01905$, $\lambda_L = 0.025$	50

Overview

Chapter 1 of this thesis is the introduction to the high multiplicity cross section problem and the idea to solve the problem using Monte Carlo simulation. Chapter 2 describes the detail of design and construction of the Beowulf parallel supercomputer. In chapter 3, the sum rules and the bound for the cross section are derived.

In chapter 4, a perturbative estimate of the critical energy is given. And the relationship between the critical energy and the Euclidean momentum on the lattice is determined. In chapter 5, the Monte Carlo simulation is described. The scaling behavior and continuum limit are also discussed. In chapter 6, I will use the perturbation method to calculate the cross sections. Chapter 7 presents the results from the simulation. Finally, I will compare the results with the perturbative calculations and discuss conclusions.

Chapter 1

Introduction

In 1990, Ringwald [1] and Espinosa [2] presented a calculation of possible instanton induced baryon number violation accompanied by enhanced production of large number of Higgs and W,Z bosons at high energy($E \sim n/g$, where n is the number of outgoing particles and g is a generic coupling constant). This has called attention to a more general and profound problem of quantum field theory. The problem is: for a given renormalized quantum field theory with weak renormalized coupling constant, what is the nature of the multi-particle production in that theory. One can think two extreme cases. In the first case, the cross section is perturbatively small [$\sim g^n \times O(1)$]. In the second case, when the number of outgoing particles $n \sim 1/g$, the multiparticle production cross section becomes unsuppressed and the inclusive cross sections saturate unitarity bounds.

It has long been known that the perturbation-theory expansion in a theory with weak coupling fails in high orders because of the factorial growth of the coefficients in the series [3]. This problem can not be solved perturbatively because the perturbation series diverges rapidly at high order. In fact, independent of the instanton calculations, Goldberg [4], Cornwall[5] and, later, Voloshin[6], Argyres, Kleiss, and Papadopoulos [7] point out that in ϕ^4 scalar field theory the contributions of just the tree graphs to the multiparticle production amplitudes gives the $n!g^n$ behavior. This suggests the possibility of the second case.

Here we have a different approach to solve this nonperturbative problem. We propose to use Monte Carlo simulation on a lattice to determine an upper bound on the cross section of the multiparticle production in ϕ_3^4 theory. The original application of this approach was to two dimensional ϕ_2^4 theory[8]. However, the case of 1 + 1 dimensions is a very special case in field theory.(no angular momentum...etc) Although the investigation in 1 + 1 dimension showed no signal of large multiparticle production, the result might be special for the 1 + 1 dimension case. In this research, we will use Monte Carlo simulation to establish a bound on the multiparticle cross section in three dimensions(1 + 2 dimensions in Minkowski). The tree diagram considerations which suggest large $1 \rightarrow n$ amplitudes in ϕ^4 are mainly combinatoric, and hold as

well in three dimensions as in two or four. Working in three dimensions has several advantages. First, we can work on large N^3 lattices as long as our computers can provide the memory and give us reasonable performance. Second, three dimensional ϕ^4 theory is a superrenormalizable theory. The wave function renormalization constant Z is finite in the ϕ_3^4 theory. The other important issue in our simulation is that we can do the simulation in three dimensional Euclidean space. The constructive quantum field theorists have proved that the ϕ_3^4 field theory exists as the analytic continuation of the continuum limit of the Euclidean lattice theory [10, 11]. In four dimensions, nonperturbatively, we would have to deal with the presumed triviality of the theory.

Even though we worked on three dimensional Euclidean lattices rather than four, the simulation itself is still a huge computing task. This is because the many degree of freedoms required for sensitivity to multiparticle production requires large lattice. For this reason, we will still need a supercomputer to do the job. To solve this problem, we built a Beowulf parallel supercomputer with sixteen CPUs. We also use the Message Passing Interface(MPI) function call to parallelize our simulation program. We are able to achieve overall 7.4 Gflops at High Performance Computing Linpack Benchmark(HPL). The theoretical peak performance for sixteen CPUs is 12 Gflops. Compare with 16 Gflops CRAY C90 at 16 CPUs, our parallel cluster has a much better price/performance ratio.

Chapter 2

Beowulf Parallel Supercomputer

2.1 The Beowulf Project History

The Beowulf Project was started by Donald Becker when he moved to CESDIS in early 1994. CESDIS was located at NASA's Goddard Space Flight Center, and was operated for NASA by USRA[12].

In the summer of 1994 the first Beowulf 16 node demonstration cluster was constructed for the Earth and Space Sciences project, (ESS). The project quickly spread to other NASA sites, other R&D labs and to universities around the world. The project's scope and the number of Beowulf installations have grown over the years. Today, the fastest Beowulf cluster can reach 143 Gflops (HPL benchmark) with 528 Pentium III 800 CPUs which ranks at 126 in the top500 supercomputer list in Nov, 2000[13]. With more and faster CPUs and even faster network links, Beowulf supercomputer can compete with any commercial high performance supercomputer such as SGI Origin 2000 or Cray T3E and costs much less.

2.2 Definition of the Beowulf Supercomputer

Beowulf is a multi computer architecture which can be used for parallel computations. It is a system which usually consists of one server node, and one or more client nodes connected together via Ethernet or some other network. It is a system built using commodity hardware components, like any PC capable of running Linux, standard Ethernet adapters, and switches. It does not contain any custom hardware components and is trivially reproducible. Beowulf also uses commodity software like the Linux or FreeBSD operating system, Parallel Virtual Machine (PVM) and Message Passing Interface (MPI). The server node controls the whole cluster and serves files to the client nodes. It might also be the cluster's console and gateway to the outside world if there is no particular annex machine. Large Beowulf machines might have

more than one server node, and possibly other nodes dedicated to particular tasks, for example consoles or monitoring stations. The client nodes in the cluster don't sit on people's desks; they are dedicated to running cluster jobs only. In most cases client nodes in a Beowulf system are dumb and are configured and controlled by the server node, and do only what they are told to do. In a disk-less client configuration, client nodes don't even know their IP address or name until the server tells them what it is. One of the main differences between Beowulf and a Cluster of Workstations (COW) is the fact that Beowulf behaves more like a single machine rather than many workstations. In most cases client nodes do not have keyboards or monitors, and are accessed only via remote login or possibly serial terminal. Beowulf client nodes can be thought of as a CPU + memory package which can be plugged in to the cluster, just like a CPU or memory module can be plugged into a motherboard. In general, the user can only login to the front end and submit their jobs to the cluster. The queueing system will receive the jobs and run them in different nodes[14].

To get better performance, one can also use some dedicated parts which can not be purchased on the commodity market. This is true especially when people need a very fast link between the nodes. One can use Giga bits Ethernet or Myrinet(240MB/s at 64-bit, 33MHz PCI) or even Quadric(340MB/s) system for the fast link. The other way to improve the floating point performance is to use DSP chips such as Texas Instrument TMS320C6xxx. These chips can boost the floating point performance up to 3 Gflops. However, the drawback is that they are expensive and some of them lack driver support.

2.3 Architecture and System Design

Our Beowulf Supercomputer is designed to solve large-scale scientific problems. Because we need to run our simulation on a large lattices, we also need huge amount of memory. Each node within the cluster is running the freely available Linux operating system. Parallel capabilities are achieved through the use of the MPI and PVM communication protocols. Job scheduling and execution for all users is handled by the Distributed Queueing System(DQS). The system contain a server node, a annex node, and 16 client nodes. All of these machines are networked by 100 BaseT Ethernet with low latency switch. (see Figure 2.1) This architecture is so call distributed memory(or local memory) architecture which is good to run both Single Program, Multiple Data(SPMD) and Multiple Instruction, Multiple Data(MIMD) program. The machine was assembled entirely from individually chosen commodity hardware components. With the exception of the Ethernet switch, all of the computer hardware within the cluster was built from the component level. This low-level approach allowed the developers to optimize the overall performance by providing us the freedom to choose the fastest and most reliable components to fit our budget. Likewise, all matters of OS and software package configuration were carried out in-house in an effort to achieve optimal settings for speed and stability[15].

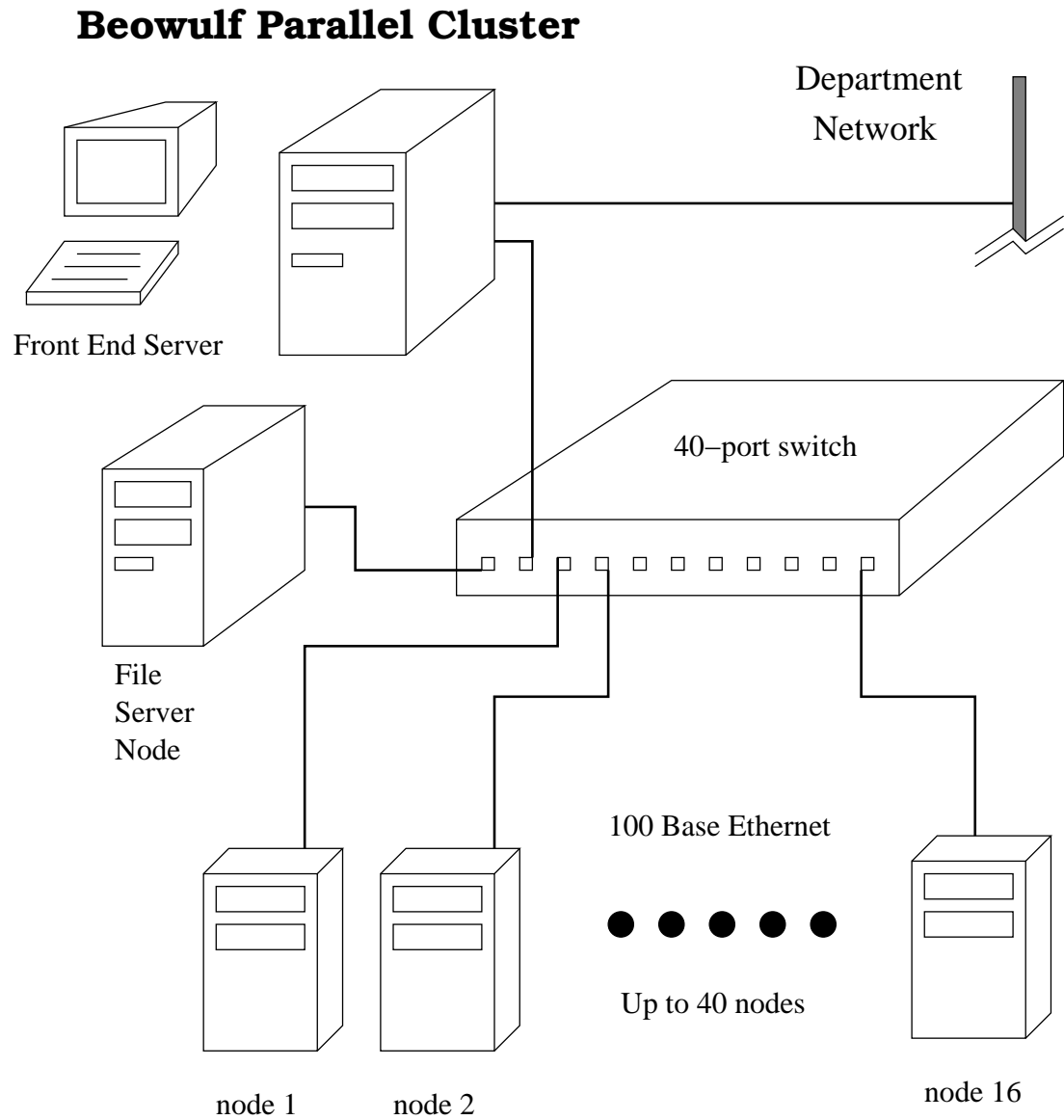


Figure 2.1: The architecture of the Beowulf Supercomputer

2.3.1 Hardware Configuration

The server node contains:

- Pentium III 500 MHz CPU
- ASUS P2B-S Motherboard
- 384 MB Samsung SDRAM
- 27 GB on two Ultra2 Wide LVD Quantum Atlas III SCSI HDs
- Seagate 12/24 GB DAT Tape Backup System
- Kingston KNE-100TX Tulip-based Ethernet card
- PCI video card
- Linksys I/O console selector switch

Each client nodes has:

- Pentium III 744 MHz Coppermine CPU
- ASUS P2B-F Motherboard
- 768 MB Micron PC133 SDRAM
- 4.3 GB UDMA Quantum Fireball HD
- Kingston KNE-100TX Tulip-based Ethernet card
- PCI video card (for boot-up only)

The annex machine is the gateway of the cluster. It has:

- ABIT BP6 Dual Celeron Motherboard with Two 450MHz CPUs
- 256 MB Samsung SDRAM
- 6 GB UDMA33 IDE HD
- Kingston KNE-100TX Tulip-based Ethernet card
- 3Com 10base-T Ethernet card (for outside LAN)
- PCI video card

2.3.2 Software Configuration

All of the nodes are running Linux Operating System. The Clients nodes share the user and utility files with the other via NFS(network file system). For the message passing protocol, we use message passing Interface(MPI), Parallel Virtual Machine(PVM), High Performance Fortran(HPF), and newly developed Cactus Code. The DQS queuing system can handle both serial and parallel jobs.

2.4 Performance and Benchmark

The performance of our Beowulf Cluster is quite remarkable. We tested it with two different parallel benchmark program which are recommended by the top500 cluster web site, NAS and HPL[16]. The NAS Parallel Benchmarks (NPB) are a set of 8 programs designed to help evaluate the performance of parallel supercomputers. The benchmarks, which are derived from computational fluid dynamics (CFD) applications, consist of five kernels and three pseudo-applications.

The detail description for each benchmark routine is following:

- CG - solution of a structured sparse linear system by the conjugate gradient method
- FT - this benchmark contains the computational kernel of a three dimensional FFT-based spectral method
- MG - Multigrid Benchmark uses a multigrid method to compute the solution of the three-dimensional scalar Poisson equation
- LU - a simulated CFD application which uses symmetric successive over-relaxation (SSOR) to solve a block lower triangular-block upper triangular system of equations resulting from an unfactored implicit finite-difference discretization of the Navier-Stokes equations in three dimensions
- IS - parallel sort over small integers
- EP - embarrassingly parallel benchmark
- SP and BT - SP and BT are simulated CFD applications that solve systems of equations resulting from an approximately factored implicit finite-difference discretization of the Navier-Stokes equations.
- BT code solves block-tridiagonal systems of 5x5 blocks; the SP code solves scalar pentadiagonal systems resulting from full diagonalization of the approximately factored scheme.

Table 2.1: NAS Benchmark

Benchmark Name	Number of Nodes	Beowulf	CRAY T3E1200 (from NAS,NASA)
BT class=C	16	1250.88 Mflops	1088.3 Mflops
IS class=C	16	28.83 Mflops	26.9 Mflops
CG class=C	16	211.63 Mflops	148.7 Mflops
EP class=C	16	52.56 Mflops	54.8 Mflops
LU class=C	16	1380.13 Mflops	1169.5 Mflops
MG class=C	16	1071.59 Mflops	1616.8 Mflops
SP class=C	16	871.19 Mflops	800.4 Mflops
FT class=C	16	392.64 Mflops	NA

Here we show the class C(large size) results in Table 2.1. Compare with CRAY T3E 1200, one can see that the Beowulf Supercomputer is even faster than T3E 1200 at same number of CPUs. However, for a heavy communication job, the T3E will be faster because of the faster interlink between the CPUs.

The second benchmark is High Performance Linpack. This benchmark is the one used in the Top500 supercomputer list[13]. HPL is a software package that solves a (random) dense linear system in double precision (64 bits) arithmetic on distributed-memory computers. It can thus be regarded as a portable as well as freely available implementation of the High Performance Computing Linpack Benchmark. Here we run three different sizes of the problem with different number of CPUs. The table 2.2 shows the results. One can see the fastest result is 7.4 Gflops at 16 CPUs(4×4). The Figure 2.2 shows that up to 16 CPUs, the speed scales up linearly. At the scale of 32 nodes or above[12], the performance saturates the bandwidth of the 100Mbits network. The Giga bits network can boost the performance more. However, the Giga bits network suffers from the TCP/IP protocol which was designed for 10Mbits network a longtime ago. For the Giga bits Ethernet link, one can only optimize either for the bandwidth or for the latency.

Table 2.2: HPL Benchmark

Matrix Size	Block size	P	Q	Time	Results(Gflops)
20000	200	2	4	1501 sec	3.55
25000	200	2	5	2324 sec	4.48
34000	200	4	4	3545 sec	7.4

HPL Benchmark Results

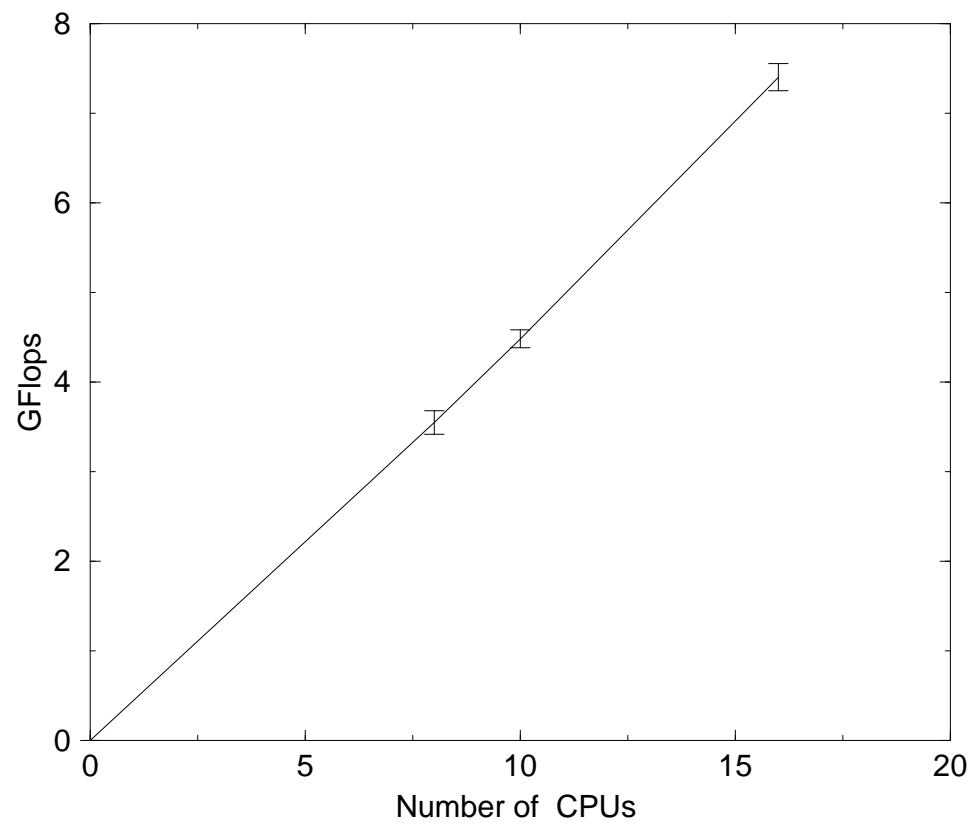


Figure 2.2: The HPL Benchmark shows the speed scales up linearly.

Chapter 3

The Cross Section and Bound

In this chapter, we want to determine the upper bound for the inclusive cross section of the multiparticle production. We will derive the bound in four steps in following four sections. First of all, we will specify the scattering process and define the inclusive cross section. Secondly, use the spectral representation of the two-point function and find the relation between the inclusive cross section and the spectral function. Thirdly, define G^{-1} , Z' , and m' and give the spectral representation of the G^{-1} function. In the last section, we will find the upper bound of the inclusive cross section.

3.1 Definition of the inclusive cross section

As we mentioned in chapter one, we want to study the amplitudes for one off-shell(time-like) ϕ particle to go to n on-shell ϕ particles (see Figure 3.1). There are the amplitudes for which extensive tree diagram analysis have been done[4, 5, 6, 7, 9]. These amplitudes may be considered as “physical” if we introduce a weak Yukawa coupling of the ϕ field to a fermion

$$\mathcal{L}_y = g_y \bar{\psi} \psi \phi, \quad (3.1)$$

and compute the cross section for $f\bar{f}$ to annihilate into $n\phi$ particles.(See Figure 3.2)

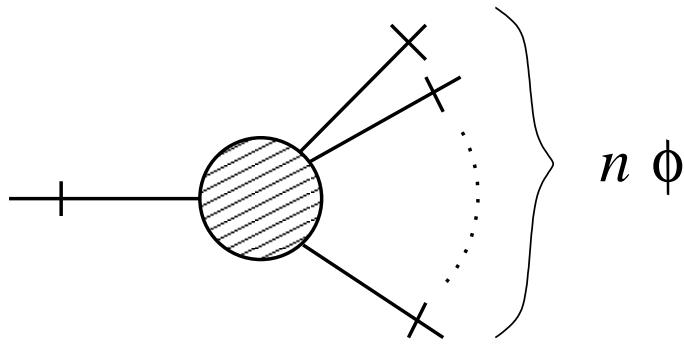
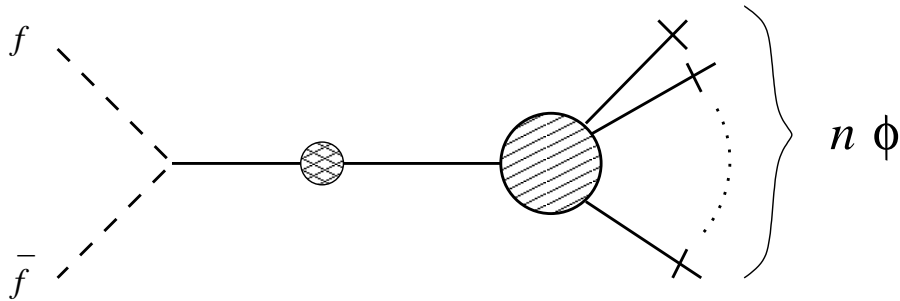
This is similar to the e^+e^- annihilation into hadrons in QCD. The transition probability for Figure 3.1 is

$$m^2 \Gamma(n, E) = \frac{1}{n!} \int d\Phi_n(E) |A(n; E)|^2 \quad (3.2)$$

where $E = \sqrt{s}$. The amplitude $A(n; E)$ is

$$A(n; E) = \underline{\mathcal{G}}_{(n+1)}(p_1, p_2, \dots, p_n) \quad (3.3)$$

which is the connected $(n+1)$ point Green function. The underscore means amputated Green function (no external line factors) and the slash means renormalized Green

Figure 3.1: The amplitude $A(n; E)$ for $\phi \rightarrow n\phi$.Figure 3.2: The amplitude for $f\bar{f} \rightarrow n\phi$, to lowest order in g_y

function (no Z factors in the Lehmann-Symanzik-Zimmermann reduction formulas). It is convenient to define a partial “cross section” of Figure 3.1 as a kinematic factor times equation 3.2

$$\sigma_n(s) = \frac{m^2}{2\pi s^2} \Gamma(n; E) \quad (3.4)$$

for n outgoing particles. The cross section of $f\bar{f} \rightarrow n\phi$ in three dimensions then can be written as (to lowest order in Yukawa coupling but to all orders in the ϕ self-coupling[7])

$$\sigma_{f\bar{f} \rightarrow n\phi}(s) = \frac{3\pi g_y^2}{8} |s Q_M'|^2 \times \sigma_n(s) \quad (3.5)$$

Finally, we include all possible number of outgoing particles and define the *inclusive cross section* as

$$\sigma(s) = \sum_n^{\infty} \sigma_n(s) \quad (3.6)$$

$$= \frac{1}{2\pi s^2} \sum_n \frac{1}{n!} \int d\Phi_n |\mathcal{G}_{(n+1)}(p_1, \dots, p_n)|^2 \quad (3.7)$$

3.2 Spectral Representation and Sum Rules

In the last section, we defined the inclusive cross section for the multiparticle final state. One can relate the inclusive cross section to the spectral function of the two point function. Let $\phi_0(x)$ be the canonical, unrenormalized scalar field in Minkowski space. We have the Wightman two point function

$$W(x, y) = \langle \Omega | \phi(x) \phi(y) | \Omega \rangle \quad (3.8)$$

The two point Green function(or τ function) is the time ordered Wightman function

$$G(x, y) = \langle \Omega | T(\phi(x) \phi(y)) | \Omega \rangle \quad (3.9)$$

Define the spectrum of physical state in three dimensions as

$$\begin{aligned} \mathbf{1} &= |\Omega\rangle\langle\Omega| + \int \frac{d^3p}{(2\pi)^3 2E_p} |p\rangle\langle p| \\ &+ \sum_{n=2}^{\infty} \frac{1}{n!} \int \prod \frac{d^3p}{(2\pi)^3 2E_n} |p_1, \dots, p_n\rangle\langle p_1, \dots, p_n| \dots \\ &= \sum_n |n\rangle\langle n| \end{aligned} \quad (3.10)$$

and the phase space integral as

$$\int d\Phi_n = (2\pi)^3 \delta^3(p_1 + \dots + p_n) \frac{1}{n!} \prod_{a=1}^n \int \frac{d^3p_a}{(2\pi)^3 2E_a} \quad (3.11)$$

The Wightman two point function has the spectral representation

$$\langle \Omega | \phi(x) \phi(y) | \Omega \rangle = \int \frac{d^3q}{(2\pi)^3} \theta(q_0) e^{-iq(x-y)} \rho(q^2) \quad (3.12)$$

$$= \int_0^{\infty} d\kappa^2 \rho(\kappa^2) \Delta^{(+)}(x-y, \kappa^2) \quad (3.13)$$

and the Green function is

$$\begin{aligned} G(x-y) &= \int_0^{\infty} d\mu^2 \rho(\mu^2) \Delta_F(x-y; \mu^2) \\ &= Z \Delta_F(x-y; m^2) + \int_{4m^2}^{\infty} d\mu^2 \rho(\mu^2) \Delta_F(x-y; \mu^2) \end{aligned} \quad (3.14)$$

where the spectral function $\rho(\mu^2)$ in three dimensions is

$$\theta(p^0) \rho(p^2) = (2\pi)^2 \sum_n \delta^3(p - p_1 - p_2 - \dots - p_n) |\langle \Omega | \phi(0) | n \rangle|^2 \quad (3.15)$$

Fourier Transform equation 3.14 and make the analytic continuation to Euclidean space.

$$\begin{aligned} G_M(p_M^2) \rightarrow G(p^2) &= \int d\kappa^2 \frac{\rho(\kappa^2)}{p^2 + \kappa^2} \\ &= \frac{Z}{p^2 + m^2} + \int d\kappa^2 \frac{\hat{\rho}(\kappa^2)}{p^2 + \kappa^2} \end{aligned} \quad (3.16)$$

$$= Z\mathcal{G}(p^2) \quad (3.17)$$

The $\hat{\rho}$ is the multiparticle($n \geq 2$) contribution to the spectral function. In three dimensions, the field strength renormalization is finite and the canonical sum rule holds:

$$1 = \int_0^\infty d\kappa^2 \rho(\kappa^2) = Z + \int d\kappa^2 \hat{\rho}(\kappa^2). \quad (3.18)$$

Positivity of the spectral function implies

$$0 \leq Z \leq 1 \quad (3.19)$$

Note that the equation 3.12 is just the Fourier transform of $\rho(q^2)$, so the inverse Fourier transform gives(choose $y = 0$)

$$2\pi\rho(q^2) = \int d^3x e^{iqx} \langle \Omega | \phi(x) \phi(0) | \Omega \rangle \quad (3.20)$$

Introduce a complete set of intermediate states 3.10 and apply the LSZ reduction formula to find

$$2\pi\rho(q^2) = G_M(q)F(q)G_M(q) \quad (3.21)$$

where

$$F(q) = \sum_n \frac{Z^n}{n!} \int d\Phi_n |\underline{\mathcal{G}}_{(n+1)}^c(p_1, \dots, p_n, q)|^2 \quad (3.22)$$

Here we only consider the connected part of the Green function. We can use equation 3.21, 3.22, and 3.7 to get the relation between σ and ρ . Define the renormalized quantities as

$$G_0 = Z\mathcal{G}, \quad \rho = Z\hat{\rho}, \quad G_{0(n+1)} = Z^{\frac{n+1}{2}}\mathcal{G}_{(n+1)} \quad (3.23)$$

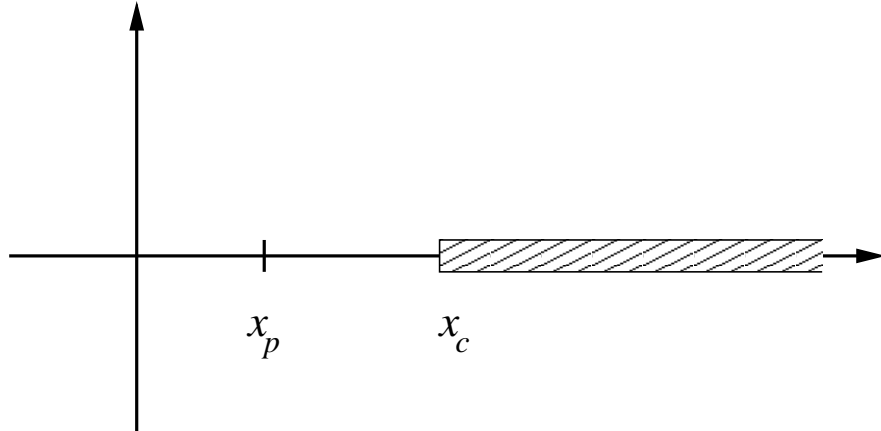
and using these equations, we find

$$\sigma(s) = \frac{\hat{\rho}(s)}{|s\mathcal{G}_M|^2} \quad (3.24)$$

3.3 Spectral Representation of G^{-1}

From equation 3.24, one can see that the inclusive cross section is closely related to the spectral function and the inverse of the Green function. The spectral representation of $G_M(P)$ in Minkowski space is

$$G_M(P) = \frac{Z}{P^2 - m^2} + \int_{4m^2}^\infty d\mu^2 \frac{\hat{\rho}(\mu^2)}{p^2 - \mu^2 + i\epsilon} \quad (3.25)$$

Figure 3.3: The pole and structure for $g(x)$

Consider a simple complex function with the same pole and cut structure as

$$g(z) = \frac{Z}{z - x_p} + \int_{x_c}^{\infty} dx' \frac{\hat{\rho}(x')}{z - x'} \quad (3.26)$$

The function has a pole at x_p and cut at $x > x_c$. The pole and cut structure are shown in Figure 3.3. To analyze the pole structure of $g^{-1}(z)$, we want to know the zero structure of $g(z)$. The positivity of ρ implies $g(z)$ has no complex zero and no zero when $x < x_p$ or $x > x_c$. The only possible zero for $g(\xi)$ is when $x_p < \xi < x_c$.

Because $g(z)g^{-1}(z) = 1$, $g^{-1}(z)$ should have the same cut structure as $g(z)$. We can write

$$g^{-1}(z) = f(z) + \sum_i \frac{\mathcal{C}_i}{z - \xi_i} + \int_{x_c}^{\infty} dx' \frac{\gamma(x')}{x' - z} \quad (3.27)$$

where \mathcal{C}_i is a positive constant and $\gamma(x)$ is the spectral function for $g^{-1}(x)$ and $f(z)$ is just a polynomial function. We can simplify the calculation by considering the case $g(z)$ has no zero ($\mathcal{C}_i = 0$). The multiple zero case will be discussed in the Appendix. So the equation 3.27 becomes

$$g^{-1}(z) = f(z) + \int_{x_c}^{\infty} dx' \frac{\gamma(x')}{x' - z} \quad (3.28)$$

Because the pole of $g(z)$ is the zero of the $g^{-1}(z)$, one can impose the condition $g^{-1}(x_p) = 0$ and $g(z)g^{-1}(z) = 1$ into equation 3.26,3.28 and get

$$g^{-1}(z) = (z - x_p) \left(1 + \int_{x_c}^{\infty} dx' \frac{\gamma(x')}{(x' - z)(x' - x_p)} \right) \quad (3.29)$$

With the $i\epsilon$ prescription of equation 3.25, we can calculate the imaginary part of $g^{-1}(x)$

$$\Im[g^{-1}(x + i\epsilon)] = \pi\gamma(x) = -\frac{\Im[g(x)]}{|g(x)|^2} = \frac{\pi\hat{\rho}(x)}{|g(x)|^2} \quad (3.30)$$

From equation 3.24, we see that $\pi s^2\sigma(s)$ is the imaginary part of \mathcal{G}_M^{-1} .

$$\pi s^2\sigma(s) = \Im[\mathcal{G}^{-1}(s)] = Z\Im[g^{-1}(s)] = Z\pi\gamma(s). \quad (3.31)$$

Hence

$$\sigma(s) = \frac{Z\gamma(s)}{s^2} \equiv \frac{\gamma(s)}{s^2} \quad (3.32)$$

To calculate the renormalization constant Z , we use $g(z)g^{-1}(z) = 1$, letting the $z \rightarrow x_p$,

$$\frac{1}{Z} = 1 + \int dx' \frac{\gamma(x')}{(x' - x_p)^2} + \dots \quad (3.33)$$

Making the analytic continuation to Euclidean space, we have the Euclidean inverse two point Green function

$$\frac{1}{G(p)} = (p^2 + m^2) \left[1 + \int d\kappa^2 \frac{\gamma(\kappa^2)}{(\kappa^2 - m^2)(\kappa^2 + p^2)} \right] \quad (3.34)$$

Expand in power of p^2 ,

$$\frac{1}{(p^2 + \xi^2)} = \frac{1}{\xi^2} \left(1 - \frac{p^2}{\xi^2} + \frac{p^4}{\xi^4} + \dots \right), \quad (3.35)$$

we have

$$\begin{aligned} G^{-1}(p^2) &= m^2 \left(1 + \int d\kappa^2 \frac{\gamma(\kappa^2)}{(\kappa^2 - m^2)\kappa^2} \right) \\ &+ p^2 \left(1 + \int d\kappa^2 \frac{\gamma(\kappa^2)}{\kappa^4} \right) \\ &+ p^4 \left(- \int d\kappa^2 \frac{\gamma(\kappa^2)}{\kappa^6} \right) + \dots \end{aligned} \quad (3.36)$$

$$\equiv \frac{1}{Z'} (m'^2 + p^2 + (\dots)p^4 + \dots) \quad (3.37)$$

In the last step, we define the m' and Z' . These quantities can be measured on the lattice. By taking derivatives of equations 3.16 and 3.37, we can find relations of m, m' and Z, Z' as

$$m'^2 \geq m^2, \quad Z' \geq Z \quad (3.38)$$

3.4 Upper Bound of Inclusive Cross Section

From equation 3.36 and 3.37, one can calculate $\frac{1}{Z'}$

$$\left. \frac{\partial G^{-1}(p)}{\partial p^2} \right|_{p^2=0} = \frac{1}{Z'} \quad (3.39)$$

So we have

$$\frac{1}{Z'} = 1 + \int d\kappa^2 \frac{\gamma(\kappa)}{\kappa^4} \quad (3.40)$$

In equation 3.32, we have defined the renormalized $\gamma(s)$ as

$$\not\gamma(s) = Z\gamma(s) = s^2\sigma(s). \quad (3.41)$$

From the above equation and 3.40, one can derive an upper bound on the integrated inclusive cross section

$$\begin{aligned} \int ds \sigma(s) &= Z \int ds \frac{\gamma(s)}{s^2} \\ &= Z \left(\frac{1}{Z'} - 1 \right) \end{aligned} \quad (3.42)$$

$$\leq \left(\frac{1}{Z'} - 1 \right) \quad (3.43)$$

Thus $1/Z' - 1$, obtained from the lattice MC simulation of Euclidean $G(p^2)$, provides a rigorous upper bound on the inclusive cross section $\sigma(s)$. If $1/Z' - 1$, computed non-perturbatively, is close to its weak coupling perturbative value, positivity implies that all of the multiparticle production cross sections are small. If $1/Z' - 1$ is large, then the multiparticle production cross sections are making a large contribution. However, the $1/Z' - 1$ only bounds the integral. Thus even if it is large, one can not conclude that the production cross section for any particular n is large. Note that from equation 3.42 and 3.38, one can also have

$$\int ds \sigma(s) \leq \frac{Z}{Z'} \leq 1 \quad (3.44)$$

This implies that if the theory is strongly coupled ($Z \ll 1$), the inequality in 3.42 is an inefficient bound. For weak coupling case ($Z' \sim Z \sim 1$), the inequality in 3.42 is nearly saturated.

Chapter 4

Critical Energy and the Relation to Euclidean Momentum

In this chapter, I will estimate the critical energy for which the multiparticle production turns on exponentially. First, I will calculate the multiparticle cross section using a statistical calculation of the multiparticle phase space integral and estimate the critical energy from the amplitude. Then I will compare the result with the direct phase space calculation for low order n . At the last, I will discuss the relation of the critical energy with the momentum on the lattice and determine the condition for the lattice simulation to be sensitive to the hypothetical large cross section for high multiplicity events.

4.1 Amplitude for $f\bar{f} \rightarrow n\phi$

In this section, we derive for the cross section for the production of n scalar in $f\bar{f}$ annihilation and estimate the critical energy which leads to sudden exponential growth. Several authors[4, 5, 6, 7, 9] have attempted to estimate the cross section perturbatively for the production of large number of ϕ . The most straightforward is the direct counting of graphs by a recursive construction, which we will outline here for the case of the pure ϕ^4 without the spontaneous symmetry breaking(SSB), in which the recursion relation is somewhat simpler. The calculation for the case with spontaneous symmetry breaking will be discussed later. For the one with SSB, we will follow Argyres, Kleiss, and Papadopoulo(AKP) and Voloshin's method [7, 6] and do the calculation in $1 + 2$ dimensions.

Consider $f\bar{f}$ annihilation into a single off-shell ϕ , which subsequently decays into n on-shell ϕ . Throughout the calculation, we only consider tree-level perturbation theory and neglect the contributions from $f\bar{f}$ annihilation into more than just one off-shell ϕ . In the pure ϕ^4 theory, symmetries phase, we can denote the number of

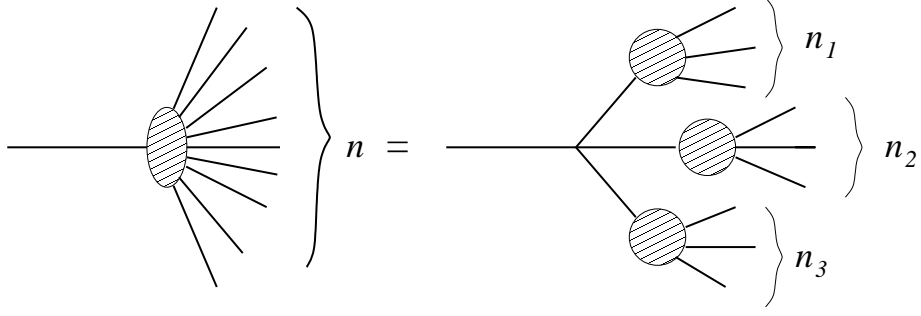


Figure 4.1: Diagrammatic structure of the recursion relation for ϕ^4 interactions in symmetry case

topologically distinct diagrams by $a(n)$. (see Figure 4.1)

$$a(n) = \lambda \frac{n!}{3!} \sum_{n_1, n_2, n_3, \text{odd}} \delta_{n_1+n_2+n_3, n} D(n_1) D(n_2) D(n_3) \frac{a(n_1)}{n_1!} \frac{a(n_2)}{n_2!} \frac{a(n_3)}{n_3!} \quad (4.1)$$

The $n!/(n_1!n_2!n_3!)$ counts the number of ways in which the n final particles can be grouped into three sets of n_1 , n_2 and n_3 particles. The δ symbol accounts for that fact that $n_1 + n_2 + n_3 = n$ and the factor $D(n_1)D(n_2)D(n_3)$ is given by the propagators D connecting the root vertex with the subtrees with n_1 , n_2 and n_3 particles in each. Note that each $a(n_i)$ can also subdecay into another three $a(n_j)$ recursively.

We consider the possible momentum configurations for the amplitude. We can find upper and lower bounds at the extreme cases of the allowed momentum configurations. For a generic momentum configuration, the recursion relation for the amplitude $a(n)$ is too complicated to deal with. We make a simplifying assumption that leads to a tractable problem. We assume that for each partition of n momentum into $n_1 + n_2 + n_3$ momentum, the average $\langle p_i \cdot p_j \rangle$ is the same for each of the momentum configurations associated with n_1 , n_2 , and n_3 . The propagator for each internal line is the same.

$$\begin{aligned} D^{-1}(n) = q^2 - m^2 &= (p_1 + p_2 + \dots + p_n)^2 - m^2 \\ &= np_i^2 + \sum'_{i,j} p_i \cdot p_j - m^2 \quad (i \neq j) \\ &= n(n-1)\langle p_i \cdot p_j \rangle + (n-1)m^2 \\ &= n^2\langle p_i \cdot p_j \rangle - n(\langle p_i \cdot p_j \rangle - m^2) - m^2 \end{aligned} \quad (4.2)$$

$$\simeq (n^2 - 1)\langle p_i \cdot p_j \rangle \quad (4.3)$$

We write

$$\langle p_i \cdot p_j \rangle = \xi^2 m^2 \quad (4.4)$$

where ξ^2 is just a positive constant. Clearly if $\xi^2 = 1$, all 3-momenta \vec{p}_i must be zero and the phase space volume vanishes. This condition gives us a trivial lower bound

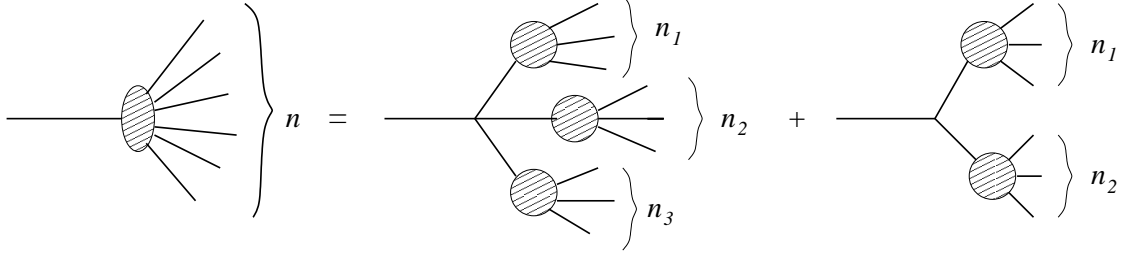


Figure 4.2: Diagrammatic structure of the recursion relation for mixed ϕ^4 and ϕ^3 interaction

on the cross section. For $\xi^2 > 1$, we have

$$D(n_i) = \frac{1}{(p_1 + p_2 + \dots + p_i)^2 - m^2} = \frac{1}{(i^2 - 1)\xi^2 m^2} \quad (4.5)$$

and the recursion relation for the amplitude becomes

$$a(n) = \frac{\lambda}{3!} \sum_{n_1, n_2, n_3, \text{odd}} \delta_{n_1+n_2+n_3, n} D(n_1)D(n_2)D(n_3) \frac{n!}{n_1!n_2!n_3!} \times \frac{a(n_1)a(n_2)a(n_3)}{(n_1^2 - 1)\xi^2 m^2 (n_2^2 - 1)\xi^2 m^2 (n_3^2 - 1)\xi^2 m^2} \quad (4.6)$$

The solution of the above recursion equation for $a(n)$ is

$$a(n) = -\xi^2 m^2 (n^2 - 1) n! \left(\frac{\lambda_4}{48\xi^2 m^2} \right)^{\frac{n-1}{2}} \quad (4.7)$$

Note that, we have approximated the multiparticle amplitude depending on $p_1, p_2 \dots p_n$ to an amplitude which is a function of total energy (or total number of out going particles) only.

For the broken symmetry case, the interaction term in Lagrange is

$$\mathcal{L}_I = \frac{\lambda_3}{3!} \phi^3 + \frac{\lambda_4}{4!} \phi^4 \quad (4.8)$$

with

$$\lambda_3 = m\sqrt{3\lambda_4}, \quad \phi = v + \hat{\phi} \quad (4.9)$$

Use the same kinematic assumption in equation 4.3 and 4.4, the recursion relation for the amplitude becomes

$$a(n) = -i\lambda_4 \frac{n!}{3!m^6\xi^6} \sum_{n_1, n_2, n_3} \delta_{n_1+n_2+n_3, n} \frac{ia(n_1)}{n_1!(n_1^2 - 1)} \frac{ia(n_2)}{n_2!(n_2^2 - 1)} \frac{ia(n_3)}{n_3!(n_3^2 - 1)} - i\lambda_3 \frac{n!}{2!m^4\xi^4} \sum_{n_1, n_2} \delta_{n_1+n_2, n} \frac{ia(n_1)}{n_1!(n_1^2 - 1)} \frac{ia(n_2)}{n_2!(n_2^2 - 1)} \quad (4.10)$$

We can make an ansatz [7]:

$$a(n) = -im^2\xi^2 n!(n^2 - 1)b(n) \left(\frac{\lambda_4}{m^2\xi^2} \right)^{\frac{(n-1)}{2}}, \quad (4.11)$$

Which leads to the following equation for the $b(n)$:

$$b(n) = \frac{1}{(12)^{(n-1)/2}} \left(\left(\frac{\mu}{\xi} + \sqrt{3} \right)^n - \left(\frac{\mu}{\xi} - \sqrt{3} \right)^n \right) \quad (4.12)$$

with $b(1) = 1$. The μ in the case of spontaneous symmetry breaking is

$$\mu = \frac{\lambda_3}{m\sqrt{\lambda_4}} = \sqrt{3} \quad (4.13)$$

In the special case $\lambda_3 = 0$, one can see that the amplitude 4.11 goes back to equation 4.7. Once again, the amplitude of multiparticle production has been approximated by an amplitude which is a function of total energy only.

4.2 The Phase Space

In chapter 3, we have defined the transition probability as

$$\Gamma(n, E) = \frac{1}{mn!} \int d\Phi_n |A(p_1, \dots, p_n)|^2 \quad (4.14)$$

In last section, we have obtained an approximation of the $1 \rightarrow n$ amplitude.

$$A(p_1, p_2, \dots, p_n) \longrightarrow A(E)$$

and the problem has been simplified to the amplitude $A(E)$ times the volume of the phase space. In order to calculate the transition probability and the cross section, we have to calculate the volume of the multiparticle phase space in as accurate a manner as possible. When n becomes very large, the exact calculation becomes very difficult. So, we still need to find a good approximation method to calculate the phase space integral. One method is to use a statistical method which was developed by F. Lurcat and P. Mazur [19] and Fermi [20]. We will derive the phase-space volume based on their method. To simplify the calculation, we choose the center of mass frame(CM) for our phase space integral.

$$P^\mu = (P^0, \vec{P}) = (E, 0)$$

where

$$P^\mu = \sum_i^n p_i^\mu$$

In general, the phase space integral in three dimensions has the following form:

$$\int d\Phi_n = \frac{1}{n!} \int \frac{d^3 p_1}{(2\pi)^3} (2\pi) \delta(p_1^2 - m^2) \cdots \int \frac{d^3 p_n}{(2\pi)^3} (2\pi) \delta(p_n^2 - m^2) (2\pi)^3 \delta^3(\vec{P} - \sum p_i) \quad (4.15)$$

We rewrite the phase space integral as

$$\int d\Phi_n = \frac{1}{n!} \int d(PS)_n(E) \quad (4.16)$$

$$(PS)_n(E) = \frac{R_n(E)}{(2\pi)^{2n-3}} \quad (4.17)$$

and

$$R_n(p) = \prod_{r=1}^n \int d^3 p_r \delta(p_r^2 - m^2) \theta(p_r^0 - m) \delta^3(p - \sum_r p_r) \quad (4.18)$$

We use a Laplace transformation to factorize this

$$\begin{aligned} \mathcal{R}_n(a) &= \int d^3 p e^{-a \cdot p} R_n(p) \\ &= \prod_{r=1}^n \int d^3 p_r e^{-a \cdot p_r} \delta(p_r^2 - m^2) \theta(p_r^0 - m) \\ &\equiv (m\varphi_0(a))^n \end{aligned} \quad (4.19)$$

where

$$m\varphi_0(a) = \int d^3 p_i e^{-a \cdot p_i} \delta(p_i^2 - m^2) \theta(p_i^0 - m) \quad (4.20)$$

for each single particle. We can define the single particle probability distribution function(**spd**) of momentum in phase space as

$$u(a, p_i) = \frac{e^{-a \cdot p_i} \delta(p_i^2 - m^2) \theta(p_i^0 - m)}{m\varphi_0(a)} \quad (4.21)$$

so that

$$\int d^3 p_i u(a, p_i) = 1 \quad (4.22)$$

Suppose the n individual momentum $p_{1,2,\dots,n}$ are independent variables and $P = p_1 + p_2 + \cdots + p_n$. From the statistical theory, we can define the full(all particles) distribution function as

$$U_n(a, P) = \frac{R_n(P) e^{-a \cdot P}}{\mathcal{R}_n(P)} = \frac{R_n(P) e^{-a \cdot P}}{(m\varphi_0(a))^n} \quad (4.23)$$

$$= \prod_{r=1}^n \frac{(\int d^3 p_r \delta(p_r^2 - m^2) \theta(p_r^0 - m) e^{-a \cdot p_r}) \delta^3(P^\mu - \sum_r p_r^\mu)}{(m\varphi_0(a))^n} \quad (4.24)$$

$$= \prod_{r=1}^n \left(\int d^3 p_r u(a, p_r) \right) \delta^3(P^\mu - \sum_r p_r^\mu) \quad (4.25)$$

We have

$$\int d^3 p U_n(a, P) = 1, \quad U_n(a, P) = \prod_r^n u(a, p_r) \quad (4.26)$$

From equation 4.17 and 4.23, we see that if we know the distribution function $U_n(a, p)$, we can calculate the $R_n(a, p)$ and the phase space (PS) integral. The $U_n(a, p)$ can be calculated by using the central limit theorem. For large n , the sum of the n independent variables ($P = p_1 + p_2 + \dots + p_n$) will have a probability distribution $U_n(a, P)$ approaching to the Gaussian. So we can expand $U_n(a, P)$ as

$$U_n(a, P) = \Psi_G(P) \left(1 + \frac{C_1}{\sqrt{n}} + \frac{C_2}{n} + \dots \right) \quad (4.27)$$

where

$$\Psi_G(P) = \prod_{\mu=0,1,2} \frac{1}{\sqrt{2\pi(\Delta P^\mu)}} e^{\left(-\frac{(p^\mu - \langle P^\mu \rangle)^2}{2\Delta P^\mu} \right)} \quad (4.28)$$

The C_1, C_2 are constants and ΔP^μ is the variation of P^μ , and $\langle P^\mu \rangle$ is the expectation value of P^μ . In the CM frame, $P^\mu = (P^0, 0)$ and $a \cdot P = (aP^0, 0)$. The trick is now to obtain a closed-form approximation for $\Psi(P)$ and then to put P^μ to its desired value $P^0 = \sqrt{s}$, $\vec{P} = 0$. The expectation value of P^1 and P^2 is zero ($\langle P^1 \rangle = \langle P^2 \rangle = 0$). Then

$$\begin{aligned} \langle p^0 \rangle &= nm \frac{\varphi_1(a)}{\varphi_0(a)} \\ \Delta P^0 &= nm^2 \left[\frac{\varphi_2(a)}{\varphi_0(a)} - \left(\frac{\varphi_1(a)}{\varphi_0(a)} \right)^2 \right] \\ \Delta P_1 = \Delta P_2 &= \frac{nm^2}{2} \left(\frac{\varphi_2(a)}{\varphi_0(a)} - 1 \right) \end{aligned} \quad (4.29)$$

with the definition of φ_1, φ_2 as

$$m^2 \varphi_1(a) = \int d^3 p_i \delta(p_i^2 - m^2) \theta(p_i^0 - m) e^{-ap_i^0} p_i^0 \quad (4.30)$$

$$m^3 \varphi_2(a) = \int d^3 p_i \delta(p_i^2 - m^2) \theta(p_i^0 - m) e^{-ap_i^0} (p_i^0)^2 \quad (4.31)$$

In the CM frame, $P^\mu = (P^0, 0)$, the expectation value of P^1, P^2 is zero. Note that the asymptotic series of $U_n(a, P)$ is formally good for any P^μ but useful only very close to the peak of the Gaussian. We therefore can tune the constant a such that $\langle P^0 \rangle = \sqrt{s}$. So, if we choose $\langle P^0 \rangle = \sqrt{s} = P^0$, the exponential function equal one and the multiparticle distribution function becomes

$$U_n(a, P) = \frac{2}{(2\pi)^{3/2} (nm^2)^{3/2} \left(\frac{\varphi_2(a)}{\varphi_0(a)} - 1 \right) \left[\frac{\varphi_2(a)}{\varphi_0(a)} - \left(\frac{\varphi_1(a)}{\varphi_0(a)} \right)^2 \right]^{1/2}} \quad (4.32)$$

and from equation 4.23, we have

$$R_n(P) = \frac{2(m\varphi_0(a))^n e^{aE}}{(2\pi)^{3/2} (nm^2)^{3/2} \left(\frac{\varphi_2(a)}{\varphi_0(a)} - 1 \right) \sqrt{\frac{\varphi_2(a)}{\varphi_0(a)} - \left(\frac{\varphi_1(a)}{\varphi_0(a)} \right)^2}} \quad (4.33)$$

So the phase space integral becomes

$$(PS)_n(E) = \frac{2(nm^2)^{-3/2}(m\varphi_0(a))^n e^{aE}}{(2\pi)^{2n-3/2} \left(\frac{\varphi_2(a)}{\varphi_0(a)} - 1\right) \sqrt{\frac{\varphi_2(a)}{\varphi_0(a)} - \left(\frac{\varphi_1(a)}{\varphi_0(a)}\right)^2}} \quad (4.34)$$

The φ_0 , φ_1 , and φ_2 can be calculated directly from equation 4.20,4.30,and 4.31

$$\varphi_0(a) = \frac{\pi e^{-am}}{am} \quad (4.35)$$

$$m^2\varphi_1(a) = \left(\frac{1}{a} + m\right) m\varphi_0 \quad (4.36)$$

$$m^3\varphi_2(a) = \left[\frac{1}{a^2} + \left(\frac{1}{a} + m\right)^2\right] m\varphi_0 \quad (4.37)$$

Note that we get the equation 4.33 and 4.34 by using a statistical method which is accurate for large n . Although our interest is in large n , is interesting to compare the R_n with the exact phase space integral at $n = 3$. For convenience, we define $1/\nu$ as the ratio of E and nm

$$\frac{E}{nm} = \frac{1}{\nu} = \frac{\varphi_1}{\varphi_0} \quad (4.38)$$

The statistical method gives us

$$\begin{aligned} R'_3 &= \left(\frac{\pi}{6}\right)^{3/2} (1 - \nu) e^3 \\ &\sim 7.61 \times (1 - \nu) \end{aligned} \quad (4.39)$$

and the exact result is

$$\begin{aligned} R_3 &= \frac{\pi^2}{2}(1 - \nu) \\ &\sim 4.93(1 - \nu) \end{aligned} \quad (4.40)$$

One can see that even at small n , the form of the dependence on ν is the same and the coefficients are the same order of magnitude. For slightly larger n , the results converge rapidly.

4.3 The Critical Energy and The relation to Lattice Momentum

The critical energy is the energy at which the transition rate begins to grow exponentially. In section 4.1 and 4.2, we have obtained the ingredients to approximate the transition rate as an amplitude squared times the phase space volume in CM frame.

$$m\Gamma(n, E) = |a(n)|^2 \frac{1}{n!} \int d\Phi_n \quad (4.41)$$

From equation 4.11 and 4.34, the n particle amplitude for the broken symmetry case is

$$A(n) \simeq -\xi^2 m^2 (n^2 - 1) n! \hat{b}(n) \left(\frac{\lambda_4}{48 \xi^2 m^2} \right)^{\frac{n-1}{2}} \quad (4.42)$$

and

$$\int d\Phi_n(E) \simeq \frac{2(nm^2)^{-3/2} (m\varphi_0(a))^n e^{aE}}{(2\pi)^{2n-3/2} \left(\frac{\varphi_2(a)}{\varphi_0(a)} - 1 \right) \sqrt{\frac{\varphi_2(a)}{\varphi_0(a)} - \left(\frac{\varphi_1(a)}{\varphi_0(a)} \right)^2}} \quad (4.43)$$

where in broken symmetry case, $\lambda_4 = 6\lambda$ and $\lambda_3 = \sqrt{3}$. So

$$\hat{b}(n) = \frac{1}{2} \left[\left(1 + \frac{1}{\xi} \right)^n - \left(-1 + \frac{1}{\xi} \right)^n \right] \quad (4.44)$$

Again, we choose the CM frame condition $\langle P^0 \rangle = P^0 = \sqrt{s} = E$. With ν defined in 4.38 and keeping just the exponential behavior, one can find the n particle transition rate is

$$\Gamma(n, E) \simeq \frac{\pi m^2}{2e} \left[(1 - \nu)^2 \times ng\nu(1 - \nu) \right]^n \quad (4.45)$$

$$= \frac{\pi m^2}{2e} e^{[n(2 \ln(1+\nu) + \ln(ng) + \ln(\nu) + \ln(1-\nu))]} \quad (4.46)$$

where we define the coupling constant

$$g = \frac{\lambda}{32\pi m} \quad (4.47)$$

and from $E^2 \simeq n^2 \xi^2 m^2$, we have

$$\xi = \frac{1}{\nu}. \quad (4.48)$$

One can see that the tree graph calculation leads to an exponentially abrupt rise of the inclusive cross section at some critical energy. If we fix n but send E to the infinity, ν will vanish as well as the transition rate. If we fix E , then n can not goes to infinity because there is not enough energy. To find the critical energy for both E and n very large, we can keep the ratio ν fixed at its maximum value and find the minimum energy of the threshold. The threshold for this blow up happens when the exponent is positive. So the critical energy E_* is the root of the exponent. Set the energy parameter $\epsilon = gE/m$ so that

$$\epsilon\nu = ng \quad (4.49)$$

Exponential growth occurs for

$$\epsilon\nu^2(1 - \nu)(1 + \nu)^2 \geq 1. \quad (4.50)$$

The function $\nu^2(1 - \nu)(1 + \nu)^2$ has maximum value 0.431, so that the minimum value for ϵ is $\epsilon_* = 2.3198$. The critical energy is

$$E_* = 2.3198 \frac{m}{g} \quad (4.51)$$

In 1 + 2 dimension, the spectral integral 3.18 is convergent, so the dominant contributions to the spectral representation of $G(p^2)$, (Equation 3.16), come from $\hat{\rho}(\kappa^2)$ with $\kappa^2 \leq p^2$. When we compute $G(p^2)$ on the lattice, the Euclidean lattice momenta are restricted to the Brillouin zone.

$$-\frac{\pi}{a} \leq p_i \leq \frac{\pi}{a} \quad (4.52)$$

The restriction for p^2 will be

$$0 \leq p^2 \leq D \left(\frac{\pi}{a} \right)^2 \quad (4.53)$$

where D is the dimension of the lattice and a is the lattice constant. Thus for the lattice calculation to be sensitive to $\sigma(s)$ for s up to E_*^2 , we must work on a lattice satisfying

$$E_*^2 \leq D \left(\frac{\pi}{a} \right)^2 \quad (4.54)$$

Dividing by m^2 , the requirement is

$$D \frac{\pi^2}{m_L^2} > \left(\frac{E_*}{m} \right)^2. \quad (4.55)$$

where $m_L = ma$ is the mass in lattice units, which is measurable on the lattice, and tends to zero as the bare parameters are tuned to approach criticality (continuum limit). Define the correlation length in the lattice units $\xi = 1/m_L$ which should satisfy

$$\frac{E_*}{\sqrt{3}\pi m} \leq \frac{1}{m_L} = \xi_L \quad (4.56)$$

in three dimensions.

For a finite lattice calculation to give a good approximation to the continuum results in general, we should have

$$a \ll \xi = \frac{1}{m} \ll L = Na \quad (4.57)$$

Use equation 4.51, 4.56 one can find the condition

$$1 \ll 74.24 \frac{m}{\sqrt{3}\lambda} < \xi \ll N \quad (4.58)$$

This set of conditions restricts the range of parameters of the simulation. In order to satisfy the critical energy threshold, the correlation length from the simulation should longer than $\sim 42.86 \frac{\lambda}{m}$. For the $\lambda/m' \sim 1$ in the broken symmetry phase, this set of conditions require lattices of size 128^3 or 256^3 .

Chapter 5

Lattice Simulation

Monte Carlo simulations have become increasingly important as a tool in studying complex statistical systems and fundamental properties of quantum field theory. In this chapter, we will discuss how to measure Z' and m'^2 on the lattice using Monte Carlo method. Because we are working close to the critical line, we experience the critical slowing down problem. I will discuss the cluster update algorithm in section two. We also want to know the properties of our simulation when the lattice spacing goes to zero. So I will discuss the continuum limit of the simulation in section three. In section four, we will specify the simulation method.

5.1 Monte Carlo Simulation

The Monte Carlo simulation on the lattice is well known. We will just follow the standard way[21]. However, it is useful to review the major features of the three-dimensional theory in the parameter space we use. The Euclidean action is discretized on an N^3 lattice with lattice constant a and periodic boundary conditions. The continuum mass and coupling λ are related to the lattice parameters by $\lambda_L = \lambda a$ and $m_L = ma$. The discretized action is

$$S = \sum_{\vec{n}} \left\{ \frac{1}{2} \sum_{\hat{n}} [\phi(\vec{n} + \hat{n}) - \phi(\vec{n})]^2 + \frac{1}{2} \mu_L^2 \phi(\vec{n})^2 + \frac{1}{4} \lambda_L \phi(\vec{n})^4 \right\}, \quad (5.1)$$

where μ_L^2 is the lattice bare mass squared. The discretized Lagrangian can be written as

$$\begin{aligned} \mathcal{L} = & -\frac{1}{2} \sum_{\vec{n}} [\phi(\vec{n} + \hat{n})\phi(\vec{n}) + \phi(\vec{n})\phi(\vec{n} - \hat{n})] \\ & + \sum_{\vec{n}} \left(3 + \frac{\mu_L^2}{2} \right) \phi(\vec{n})^2 + \frac{\lambda_L}{4} \sum_{\vec{n}} \phi(\vec{n})^4 \end{aligned} \quad (5.2)$$

Since the momentum on the lattice should be inside the Brillouin zone, the discretized free propagator is

$$G_0(k) = \frac{1}{\left\{ \sum_{i=1}^3 \frac{1}{a^2} 2(1 - \cos(ak_i)) + m^2 \right\}} \quad (5.3)$$

Note that in the simulation, we didn't distinguish different lattice momentum vectors which give the same momentum magnitude, *i.e.*, $|k_{i,j,k}| = |k_{j,k,i}| = |k_{k,i,j}| \dots$ etc.

We use the Metropolis algorithm to generate a sequence of equilibrium configurations. Here we only consider the nearest neighbor interaction at each lattice site. The probability density is

$$dP(\phi) = \frac{e^{-S(\phi)}}{\mathcal{Z}} \prod_{\vec{n}} d\phi(\vec{n}) \quad (5.4)$$

where the partition function is

$$\mathcal{Z} = \prod_{\vec{n}} \int d\phi(\vec{n}) e^{-S(\phi)}. \quad (5.5)$$

A random walk goes through the phase space with the acceptance probability

$$e^{i(S_{new} - S_{old})} \quad (5.6)$$

for each change of $\phi \rightarrow \phi + d\phi$ at each lattice site. We measure the one-point and two-point functions after sweeping through the lattice. We also compute the Fourier transform of the ϕ field and calculate the two-point function in momentum space by

$$G(k) = \langle \phi(k) \phi(-k) \rangle. \quad (5.7)$$

Then at small momentum k , the reciprocal of the two point function is

$$G(k)^{-1} = \frac{1}{Z'} (m^2 + k^2 + O(k^4) \dots) \quad (5.8)$$

We then plot the reciprocal of the two-point function in momentum space against the reciprocal of the Fourier transform of the massless free lattice two-point function ($m = 0$ in 5.3). The quantities m_L^2 and Z' in equation 3.37 are extracted from the intercept and slope at the origin of this plot. To illustrate the plot, we have shown one example in Figure 5.1 . Here we plot the Monte Carlo evaluation of the free propagator ($\lambda = 0$) $G^{-1}(\vec{p})$ against the massless $G_0^{-1}(\vec{p}) = 4 \sum_{\mu} \sin^2(p_{\mu})^{-1} \equiv \vec{p}^2$. One can see that the Monte Carlo results is the same as the known analytic result equation 5.3. Note that this provides a nontrivial check of a large fraction of our Fortran programs.

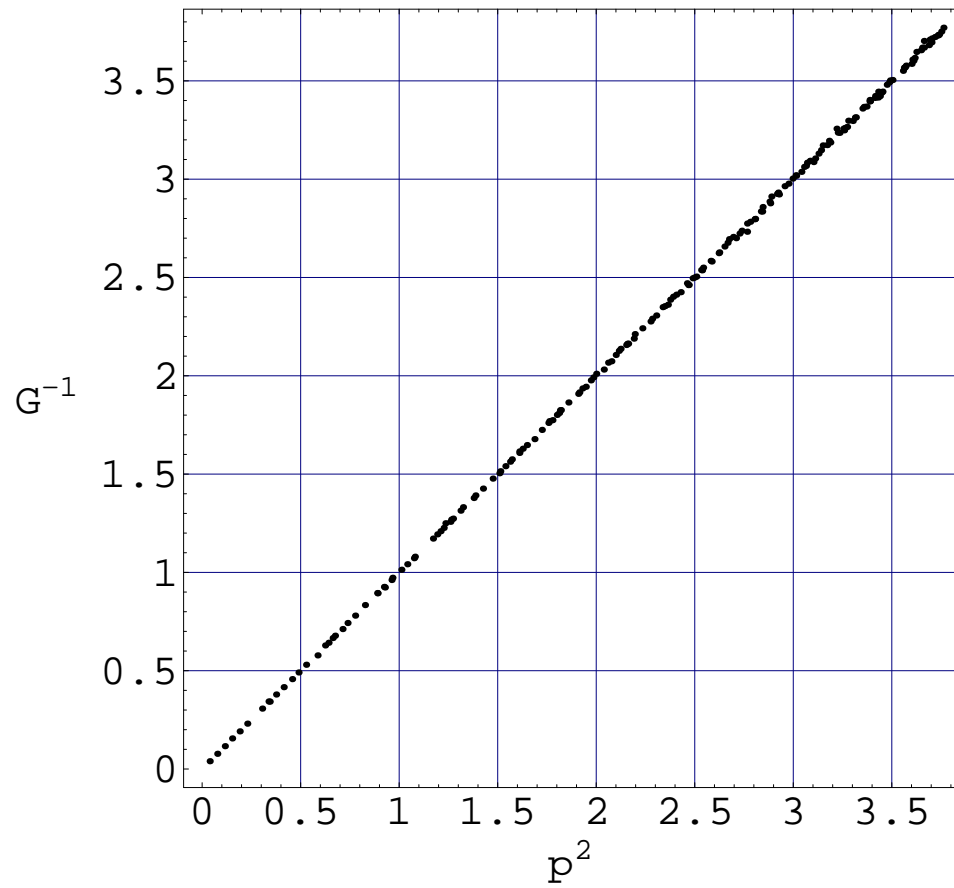


Figure 5.1: Result of Monte Carlo evaluation of $G_0^{-1}(\vec{p})$ plotted against exact analytic massless $G_0^{-1}(\vec{p}) = 4 \sum_{\mu} \sin^2(p_{\mu})^{-1} \equiv \vec{p}^2$ at 32^3 lattice. Error bars on Monte Carlo results are too small to show up on this plot.

Table 5.1: Comparison of the values of the dynamic exponent z for different algorithms for Ising model in various dimensions[28].

dimension d	Metropolis	Wolff	Swendsen-Wang
2	2.167 ± 0.001	0.25 ± 0.01	0.25 ± 0.01
3	2.02 ± 0.02	0.33 ± 0.01	0.54 ± 0.02
4	-	0.25 ± 0.01	0.86 ± 0.02

5.2 Cluster Update Algorithm

The Metropolis algorithm has a major drawback when working very close to the critical point. It suffers from critical slowing down if one approaches the phase transition. As one approaches to the critical point, both the correlation length and correlation time diverge. The relation of the correlation length ξ and correlation time τ are[27, 21]

$$\tau \sim \xi^z \sim L^D \quad (5.9)$$

where the z is so called dynamic exponent and the τ is measured in computer steps. This equation tells us how the time correlation gets longer as the correlation length diverges near criticality. However, in a system of finite size, the correlation length can never really diverge. With the lattice size L , the correlation time increase as

$$\tau \sim L^z \quad (5.10)$$

when close to the criticality. One can see that as we approach criticality, we need to have longer CPU time to get the required statistics.

To avoid the critical slowing down, one must define appropriate nonlocal(or collective) variables and a new dynamics for driving them. Progress has been made with some nonlocal algorithms for both discrete spin models and continuum fields. Swendsen and Wang[22] have used the Fortuin-Kastelyn [23] percolation map for the Potts model to define collective coordinates that allow domains to be inverted with zero free energy cost. Another approach was proposed by Wolff[24] which is essentially the same as Swendsen and Wang algorithm with some modifications. Further improvements are possible by introducing multigrid methods[25].

However, the algorithm for the ϕ^4 field theory is a little more complicated. Brower and Tamayo[26] proposed an algorithm for ϕ^4 field theory based on the Swendsen and Wang algorithm. Here we will follow Brower and Tamayo's method but switch to the Wolff algorithm. Table 5.1 compare the dynamic exponent value for the Ising model in different dimension and algorithm. One can see that the Wolff algorithm is a little better than Swendsen and Wang algorithm in three dimension.

In our simulation, the update algorithm consists basically of two parts:(**1**) a conventional Metropolis Monte Carlo update for the $\phi(x)$ field and (**2**) Wolff cluster identification and flipping. To identify the cluster of ϕ field, one can introduce a

discrete variable $s_{\vec{n}}$ to describe the Ising like property of the field ϕ ,

$$\phi(\vec{n}) = s_{\vec{n}}|\phi(\vec{n})| \quad (5.11)$$

where the $s_{\vec{n}} = \pm 1$.

The detailed procedure is as follows:

- (1). Update the $\phi(\vec{n})$ fields via a standard local Monte Carlo algorithm. In our case, it is the Metropolis algorithm.
- (2). Choose a site \vec{n} at random from the lattice.
- (3). At that chosen site, \vec{n} , introduce an effective Ising-type system,

$$e^{-S_{Ising}} = \prod_{\vec{n}, \vec{n}+\hat{n}} e^{|\phi(\vec{n})\phi(\vec{n}+\hat{n})|(s_{\vec{n}}s_{\vec{n}+\hat{n}}-1)} \quad (5.12)$$

and look in turn at each of the neighbor of that ϕ . Add the neighbor $\phi(\vec{n} + \hat{n})$ to the cluster with the probability

$$P_{add} = 1 - e^{-|\phi(\vec{n})\phi(\vec{n}+\hat{n})|(1+s_{\vec{n}}s_{\vec{n}+\hat{n}})} \quad (5.13)$$

$$= 1 - e^{-(|\phi(\vec{n})\phi(\vec{n}+\hat{n})|+\phi(\vec{n})\phi(\vec{n}+\hat{n}))} \quad (5.14)$$

Note that $P_{add} = 0$ if $\phi_{\vec{n}}$ and $\phi_{\vec{n}+\hat{n}}$ have opposite sign. That is, we only add the neighbors to the cluster when they have the same sign as the chosen one.

- (4). From the boundary of the cluster, repeat the adding step in (3) as many times as necessary until there are no ϕ left in the cluster whose neighbors have not been considered for inclusion in the cluster.
- (5). Flip the sign of the cluster.

The beauty of the Swendsen-Wang and Wolff update step is that the entropy of the percolated cluster formation exactly cancels the surface energy to give zero free-energy cost. Detailed balance is guaranteed by the condition that summing out the percolation variables in the joint distribution, P_{add} , of equation 5.14 yields the correct Ising distribution of equation 5.12. With the Wolff algorithm, our autocorrelation of the VEV has been reduced from ~ 400 to ~ 2 . Figure 5.2 shows the differences of the simulation results with and without the cluster update algorithm. The simulation without the cluster update algorithm has six millions sweeps whereas the one with the cluster update only needs hundred thousand sweeps.

5.3 Continuum Limit

The continuum ϕ^4 quantum field theory can be recovered from a discrete lattice theory by taking the limit of the lattice constant a going to zero and possibly rescaling the

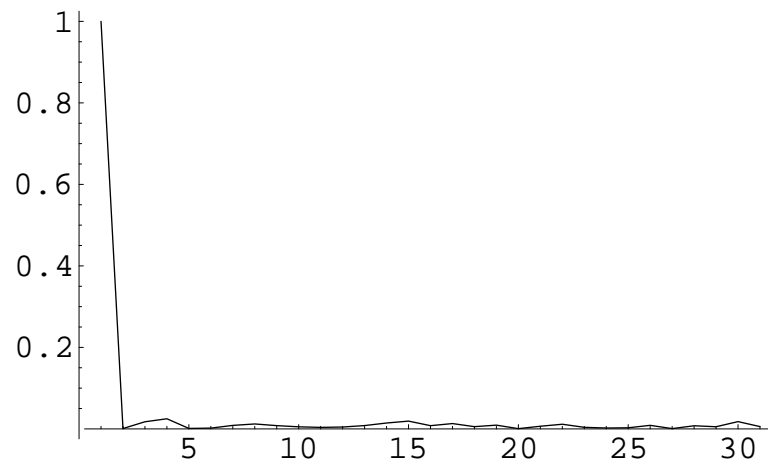
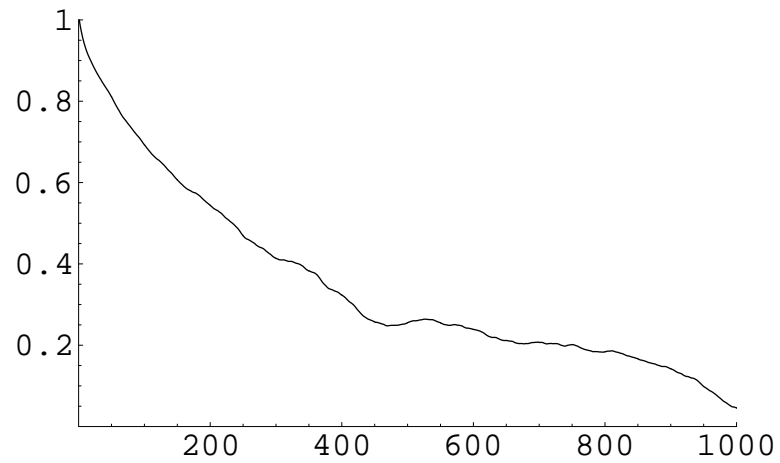


Figure 5.2: The autocorrelation for the $\langle\phi\rangle$ with and without the cluster update algorithm. The e^{-1} point for the one without the cluster update algorithm is at about 400(top). The autocorrelation length for the one with cluster update algorithm is about 2 only(bottom).

field strength by a factor of $Z(a)$. The existence of the limit of the lattice ϕ^4 theory in three dimension has been proved by R. Fernández, J. Fröhlich and A. Sokal[11], and J. Glimm and A. Jaffe [10]. To make use of the simulation, we have to know the behavior of the theory as $a \rightarrow 0$.

In ϕ^4 theory on the lattice, we have defined the $\lambda_L = \lambda a$ and $m_L = ma$ which measured in lattice units. The correlation length in physics units is $\xi = 1/m$. The correlation length of the lattice units is $\xi_L = \xi/a = 1/m_L$. Consider a simulation on a linear lattice of N_1 lattice point(in figure 5.3, $N_1 = 8$). Suppose the simulation with initial parameters $\{P_1\}$ gives output correlation length in lattice units ξ_{L_1} (in figure 5.3, $\xi_{L_1} = 4$). In the computer simulation all quantities are in lattice units; there is no physical lattice spacing. We are free to introduce a lattice constant a_1 in some arbitrary physical units. Then the correlation length in physical units is $\xi_1 = \xi_{L_1} \times a_1 (= 4a_1)$. We now want to proceed toward the continuum limit $a_\infty \rightarrow 0$. We do this by a sequence of halving the *physical* lattice spacing, as follows: Go to lattice of $N_2 = 2N_1 (= 16$ in figure 5.3) lattice points. Adjust the input parameters $\{P_2\}$ so that the output correlation length in lattice units in $\xi_{L_2} = 2\xi_{L_1} (= 8)$. As the figure shows, this may be interpreted a $a_2 = a_1/2$ and $\xi_2 = \xi_{L_2} \times a_2 = \xi_1$, *i.e.* we have halved the *physical* lattice spacing while keeping the physical volume and the correlation length in physical units fixed.

When a goes to zero, we have

$$a \longrightarrow 0 \tag{5.15}$$

$$\xi_L \longrightarrow \infty, \tag{5.16}$$

$$m_L \longrightarrow 0 \tag{5.17}$$

For the λ , we have two different possibilities[11]:

- (1) λ *fixed*, so that when $a \rightarrow 0$, $\lambda_L \rightarrow 0$. This is the standard procedure in super-renormalizable field theory($d < 4$). From the point of view of field theory, no nontrivial coupling-constant renormalization is being performed; and none need be performed, since there is no ultraviolet divergences for the coupling constant renormalization in $d < 4$. From the point of view of statistical mechanics, the theory is becoming extremely *weakly* coupled($\lambda_L \sim a^{4-d}$); but the effects of this coupling are amplified by the *infrared* divergences of the ϕ^4 lattice theory near the critical point in $d < 4$, leading to a non-Gaussian continuum limit.
- (2) λ_L *fixed*, so that when $a \rightarrow 0$, $\lambda \rightarrow \infty$. This is the standard procedure in the statistical mechanical theory of critical phenomena. In this case it is for $d > 4$ that matters are simple: correlation function are given by a perturbation expansion that is free of infrared divergences. From the point of view of field theory this might seem surprising, since the ϕ_d^4 field theory for $d > 4$ is perturbatively non-renormalizable, with horrendous ultraviolet divergence. However, it is mitigate by the fact that the theory is becoming extremely *weakly* coupled($\lambda \sim a^{d-4}$).

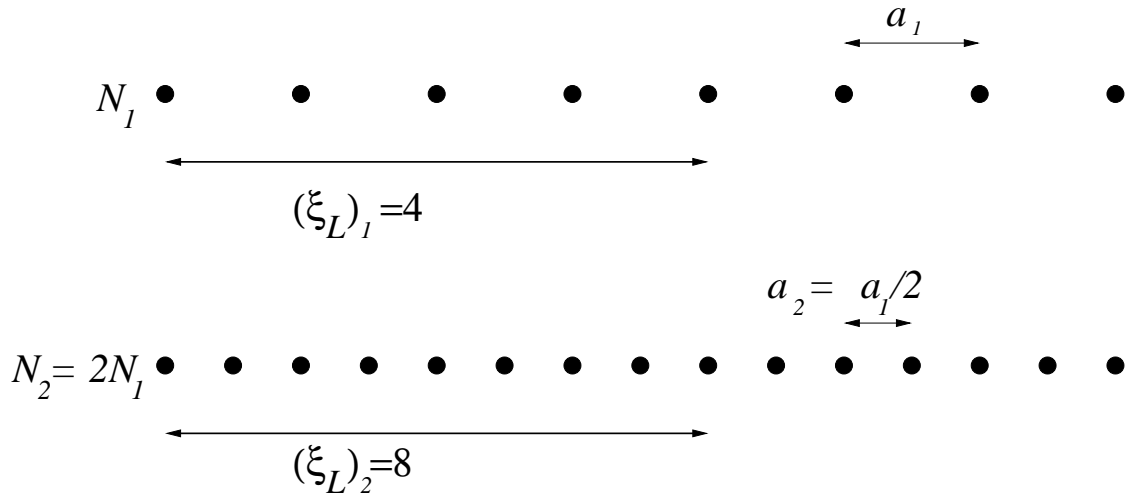


Figure 5.3: The scaling of the continue limit. When we halve the lattice constant, $a \rightarrow a/2$, the correlation length, ξ_L , will be doubled $\xi_L \rightarrow 2\xi_L$

On the other hand, for $d < 4$ the theory of critical phenomena is very complicated, by virtue of the infrared divergences. This is reflected in field theory in the fact that the theory is becoming extremely *strongly* coupled ($\lambda \sim a^{d-4}$), causing perturbation theory to break down even though the internal momentum integrations are ultraviolet convergent.

The Figure 5.4 shows the different limits in the two parameter (λ, a) plane. When $\lambda \rightarrow \infty$, that corresponds to the Ising limit. When $\lambda \rightarrow 0$, that corresponds to the Gaussian limit. When $a \rightarrow 0$, that corresponds to the continuum limit. The Figure 5.5 shows the statistical mechanical approaches for $d < 4$ and $d > 4$ (the solid lines), also for the field theory approach (the dashed arrow).

Since we want to consider a superrenormalizable theory with fixed weak coupling constant, we use the first alternative. Hence when a goes to zero, the λ_L should also goes to zero.

$$a \rightarrow 0, \quad \lambda_L \rightarrow 0 \quad (5.18)$$

In the simulation, when we halve the lattice constant $a \rightarrow a/2$, we should have $\lambda_L \rightarrow \lambda_L/2$ and $\xi_L \rightarrow 2\xi_L$.

The phase diagram of the theory in terms of the parameters μ_L^2 and λ_L is sketched in Figure 5.6. The Gaussian fixed point at $(\mu_L^2, \lambda_L) = (0, 0)$ is not trivial in less than four dimensions, as has been demonstrated by constructive field theory techniques [10, 11]. The physical dimensionful coupling constant remains finite as this Gaussian fixed point is approached along the dashed or dotted lines sketched in Figure 5.6. The solid line extending outward from the origin is the line of the second-order phase transition separating the broken symmetry phase from the symmetric phase. In this space of

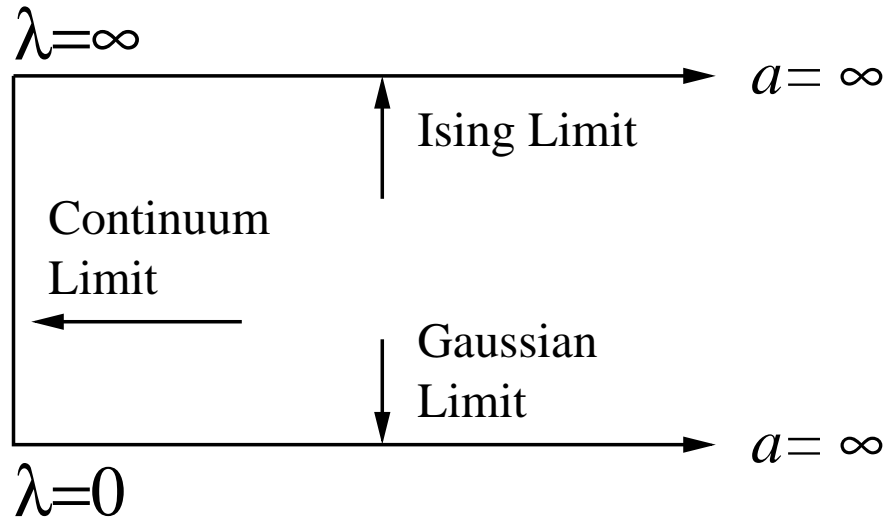


Figure 5.4: The two parameters (λ, a) phase diagram for different limits

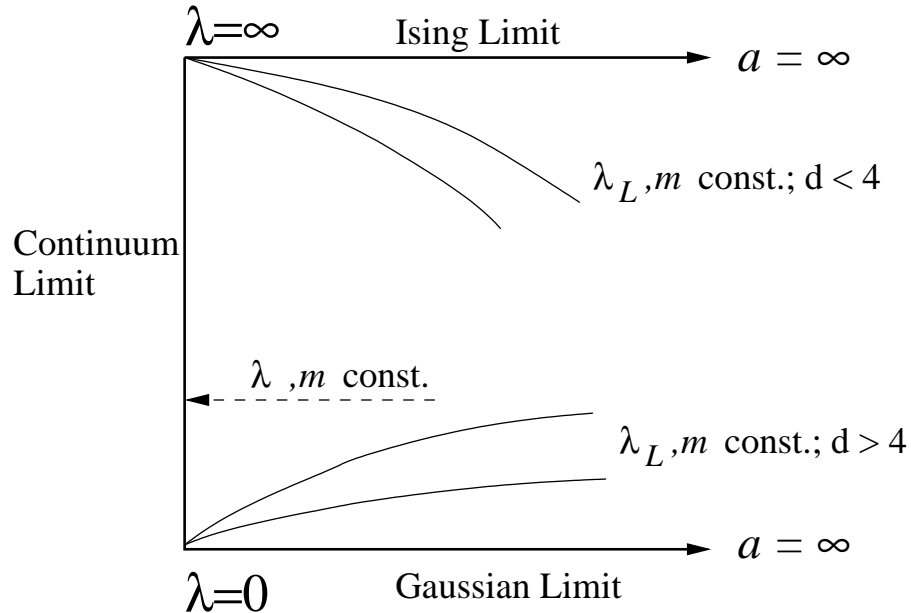


Figure 5.5: The two parameters (λ, a) phase diagram. The diagram shows the statistical mechanical approach for both $d < 4$ and $d > 4$. The dashed arrow shows the field theory approach.

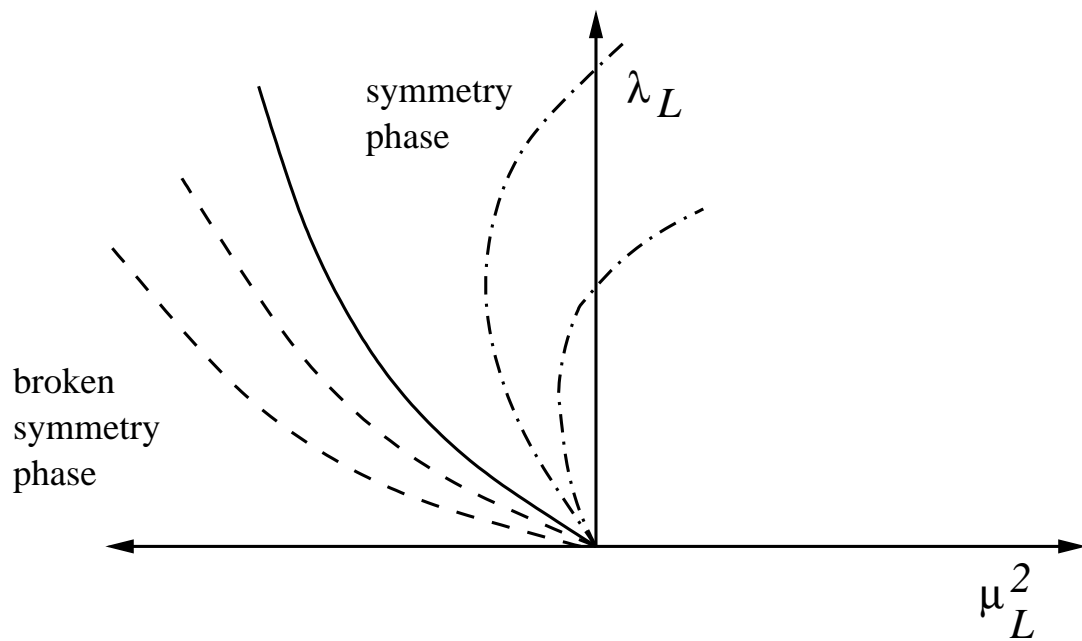


Figure 5.6: The phase diagram for the three-dimensional, single component scalar ϕ^4 theory. The solid line separates the symmetric phase from the broken symmetry phase. The dash-dot lines represent lines of constant physics in the symmetry phase, and the dashed lines are lines of constant physics in the broken phase. The origin is the Gaussian limit and does not imply a trivial field theory for $d < 4$.

the lattice coupling constant and lattice bare mass squared, continuum physics is recovered by moving toward the origin along line determined by the renormalization group flow. Along these lines the ratio of the renormalized coupling and mass are constant. We want to emphasize that we are not working near the Ising fixed point, which in this parameterization is the point on the solid line with $\lambda_L \rightarrow \infty$.

Other dimensionless properties $\{P\}$ of the system should also remain fixed when we approach to the continuum limit. One expects to approach the continuum limit for $\xi_L \gg 1$. If one starts far from continuum limit (ξ_L not $\gg 1$), the $\{P\}$ will not stay fixed (within statistical errors) until after a number of steps have got to large enough ξ_L (see figure 5.3). When this has been achieved, one claims that one is so close to the continuum limit values of the $\{P\}$ that error due to lattice contamination is less than the statistical error of the simulation.

5.4 The Simulation Methods

Here we describe step by step how we carry out the simulation and analysis the data. Because we know the continuum limit of $1/Z'$ and m' exists [10, 11], we will try to halve the lattice constant a until those values settle to their continuum limits (invariant under $a \rightarrow a/2$). The method is:

- (1). Choose the proper values for λ_L and $\mu_{0_L}^2$ as the input parameters and calculate the $1/Z'$ and m'^2 by measuring the slope and intercept of the G^{-1} plot in section 5.1.
- (2). Then we check whether the correlation length ξ_L satisfying the conditions in equation 4.58 or not.
- (3). If it satisfies the condition, then the value of $1/Z'$ will gives us the upper bound of inclusive cross section.
- (4). If not, we halve our lattice space (go to higher energy but fix the ratio of E/n) and, according to the continuum limit, move to the the next point on the phase diagram along the dash line in Figure 5.6. In our simulation, halving the lattice constant and keep the volume fixed is the same as keeping the lattice constant fixed and double the lattice size. So we have $N \rightarrow 2N$ and set $\lambda_L \rightarrow \lambda_L/2$ then find the proper value of $\mu_{0_L}^2$ (actually, $\mu_{0_L}^2 \rightarrow \mu_{0_L}^2/2$ approximately)¹ to makes $\xi_L \rightarrow 2\xi_L$. Under this condition, we keep the dimensionless quantity λ/m' the same. This step will guarantee we stay on the dash line in Figure 5.6 but moves close to the origin.
- (5). At this new scale, measure the $1/Z'$ and m' and check the condition 4.58 again. If the correlation length still can not satisfy the condition or it satisfies but the

¹This is because in 3-D ϕ^4 theory, the bare mass square, $\mu_{0_L}^2$, is linearly UV divergent and propotional to m_L and when $a \rightarrow a/2$, $m_L \rightarrow m_L/2$.

values $1/Z'$ and m' do not remain the same, we then repeat step (4) until the correlation length can satisfy the equation 4.58 and both $1/Z'$ and m' do not change anymore.(stay within estimated errors bounds)

The last step checks the continuum limit of the simulation. If $1/Z'$ and m' are insensitive to the lattice space, the value will be very close to the continuum limit(with some statistical errors). In the real life, we can not keep enlarging the lattice size because of the limit of our computing power. We can only choose the starting point by try and error at small lattice size $N = 32$, then move up to the maximum lattice size $N = 256$.

5.5 Verify the Ising limit of the Simulation

From Figure 5.4, one can see that if the λ in the ϕ^4 theory goes to infinity, it becomes the Ising theory. The Ising model Monte Carlo simulation have been well known in statistical mechanics [29, 30]. To verify our Monte Carlo simulation in three dimension ϕ^4 theory, one can compared the results of three dimensional ϕ^4 at Ising limit ($\lambda \rightarrow \infty$) with the results from Ising model simulation. It is well known that the critical temperature β_c for the three dimensional Ising model is about $\beta_c = 0.2217$. The ϕ^4 theory should be able to reproduce this result by letting the $\lambda \rightarrow \infty$. We can rewrite the field theory Lagrangian 5.2 as

$$\mathcal{L} = - \sum_{\vec{i} \neq \vec{j}} \phi_{\vec{i}} \phi_{\vec{j}} + \sum_{\vec{i}} \frac{\lambda}{4} \left(\phi_{\vec{i}}^2 - \frac{-\mu_L^2 + 2d}{\lambda} \right)^2 \quad (5.19)$$

where the d is the dimension. When $\lambda \rightarrow \infty$, it should goes back to the Ising model. Compare with the Hamiltonian of Ising model

$$\mathcal{H} = -\beta \sum_i \sigma_i \sigma_j, \quad (5.20)$$

we see that the $\lambda \rightarrow \infty$ will force the second term in equation 5.19 to zero. So, we can have

$$\lim_{\lambda \rightarrow \infty} \phi_{\vec{i}}^2 - \frac{-\mu_L^2 + 2d}{\lambda} = 0 \quad (5.21)$$

This suggest that

$$\lim_{\lambda \rightarrow \infty} \phi_{\vec{i}} = \pm \sqrt{\frac{-\mu_L^2 + 2d}{\lambda}} \equiv \sqrt{\beta} \sigma_{\vec{i}} \quad (5.22)$$

where the $\sigma_{\vec{i}} = \pm 1$ and

$$\beta = \frac{-\mu_L^2 + 2d}{\lambda} \quad (5.23)$$

Under this limit, the Hamiltonian of ϕ^4 theory becomes

$$\mathcal{H} = \lim_{\lambda \rightarrow \infty} \sum_{\vec{i} \neq \vec{j}} \phi_{\vec{i}} \phi_{\vec{j}} - \sum_{\vec{i}} \frac{\lambda}{4} \left(\phi_{\vec{i}}^2 - \frac{-\mu_L^2 + 2d}{\lambda} \right)^2$$

Table 5.2: The Monte Carlo simulation of $32^3 \phi_3^4$ theory at Ising limit($\lambda \rightarrow \infty$). The table shows the critical temperature β_c at different λ values.

λ	$\mu_{0_c}^2$	$-\frac{\mu_{0_c}^2}{\lambda}$	β_c
100	-31	.31	.25
300	-75	.25	.23
1000	-228	.228	.222

$$= -\beta \sum_{\vec{i} \neq \vec{j}} \sigma_{\vec{i}} \sigma_{\vec{j}} \quad (5.24)$$

which is the Ising model with the external field $J = 0$.

To verify the Ising limit, we do the simulation with the $\lambda \gg 1$ and calculate the VEV $\langle \phi \rangle$ for different μ_0^2 . We start in the symmetric phase with one λ value and change the value μ_0^2 until the VEV is no longer zero. In our simulation, when $\lambda \gg 1$, we get a very sharp transition from the symmetric phase to broken symmetry phase. So, it is very easy to identify the critical $\mu_{0_c}^2$. Table 5.2 shows the β_c from the simulation at 32^3 with different λ . The third row shows that when $\lambda = 1000$, the β_c is very close to the value 0.2217. This give us confidence in our simulation.

Chapter 6

The Perturbation Calculation

6.1 ϕ_3^4 model and renormalization

To compare with the simulation results, we have done the perturbation calculation for the VEV, $\langle\phi\rangle/\sqrt{m'}$, and $1/Z'$ in three dimensional ϕ^4 theory. We use the standard Lagrangian

$$\mathcal{L} = \frac{1}{2}\partial\phi_0(x)\partial\phi_0(x) - \frac{\mu_0^2}{2}\phi_0^2(x) - \frac{\lambda_0}{4}\phi_0^4(x) \quad (6.1)$$

The field are unrenormalized canonical field, and μ_0^2 , λ_0 are bare mass and coupling constants. To implement perturbation theory in the broken symmetry phase($\mu_0^2 < 0$, $\langle\phi\rangle \neq 0$), the field is shifted

$$\langle\phi_0\rangle = \mathcal{V}_0, \quad \phi_0 = \mathcal{V}_0 + \hat{\phi}_0 \quad (6.2)$$

The condition that one is perturbing about the correct vacuum is

$$\langle\hat{\phi}_0\rangle = 0 \quad (6.3)$$

This condition determines \mathcal{V} as a function of the parameters of the theory. The bare field and parameters are renormalized as

$$\phi_0 = \sqrt{Z}\phi, \quad \mu_0^2 = Z_m\mu^2, \quad \mathcal{V} = \sqrt{Z}V \quad (6.4)$$

As we mentioned before, in three dimension super renormalizable theory, there is no need to renormalize the coupling constant λ . Hence we can set

$$\lambda_0 = \lambda, \quad Z_\lambda = 1 \quad (6.5)$$

When we substitute the renormalized field in to the bare Lagrangian, and write all Z 's as $Z = 1 + \delta Z$, one can get a renormalized Lagrangian plus terms proportional to V (and containing no δZ), plus counter terms which are proportional to one or more δZ 's. To implement the stability condition 6.3, compute the tadpole graphs,

including counter terms, to a given order(number of loops) in perturbation theory, and expand the renormalized V

$$V \equiv \zeta_v v, \quad (6.6)$$

$$\zeta_v = 1 + \zeta_v^{(1)} + \zeta_v^{(2)} + \dots \quad (6.7)$$

and adjust ζ_v (equivalently V) to satisfy 6.3 order by order. In the broken symmetry phase, we can expand the linear $\hat{\phi}$ term in the Lagrangian(up to one loop order)

$$\mathcal{L} = -(\mu_0^2 + \lambda V^2)V\hat{\phi}_0 \quad (6.8)$$

$$= -(Z_m\mu^2 + Z\zeta_v^2\lambda v^2)Z\zeta_v v\hat{\phi} \quad (6.9)$$

$$= -(\mu^2 + \lambda v^2)v\hat{\phi} - (\mu^2 + \lambda v^2)(\zeta_v - 1)v\hat{\phi} \\ - [(Z_m Z - 1)\mu^2 + (Z^2\zeta_v^2 - 1)\lambda v^2]v\hat{\phi}/ \quad (6.10)$$

$$+ \text{two-loop counter terms} \quad (6.11)$$

The zeroth order fixes

$$v^2 = -\frac{\mu^2}{\lambda}, \quad (\mu^2 = -\frac{m^2}{2} < 0) \quad (6.12)$$

and the one loop counter term may be written as

$$\mathcal{L}_1 = v\delta\mu^2\hat{\phi} \quad (6.13)$$

$$\delta\mu^2 = (Z_m Z - Z^2\zeta_v^2)\lambda v^2 + \text{two-loops term} \quad (6.14)$$

Computation of $\langle\hat{\phi}\rangle$ in one-loop order(Figure 6.1) give

$$\langle\hat{\phi}\rangle = -i3\lambda v A_m + iv\delta\mu^2 = 0 \quad (6.15)$$

where the regularized Feynman integral is

$$A_m = i \int \frac{d^3p}{(2\pi)^3} \frac{1}{p^2 - m^2 + i\epsilon} \quad (6.16)$$

The $\hat{\phi}^2$ terms in the Lagrangian gives

$$\mathcal{L}_2 = \partial\phi\partial\phi - \frac{m^2}{2}\hat{\phi}^2 + \frac{1}{2}\delta\mu^2\hat{\phi}^2 - \frac{m^2}{2}(Z^2\zeta_v^2 - 1)\hat{\phi}^2 \quad (6.17)$$

the one-loop counter terms(for $-i\Sigma$) generated by equation 6.17 are

$$CT = i(Z - 1)q^2 + i\delta\mu^2 - i(Z^2\zeta_v^2 - 1)m^2 \quad (6.18)$$

The one-loop self-energy diagrams are shown in Fig. 11. The tadpole diagram plus the tadpole counter term add to zero by our previous choice of $\delta\mu^2$. Hence, the renormalized self-energy function is

$$-i\Sigma(q^2) = -i18\lambda^2 v^2 I_{mm}(q^2) + i\delta Z q^2 - i(Z^2\zeta_v^2 - 1)m^2 \quad (6.19)$$

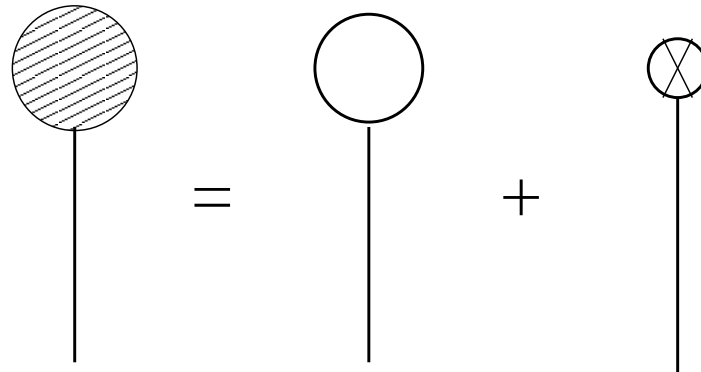


Figure 6.1: The one-loop tadpole diagram and the counter term.

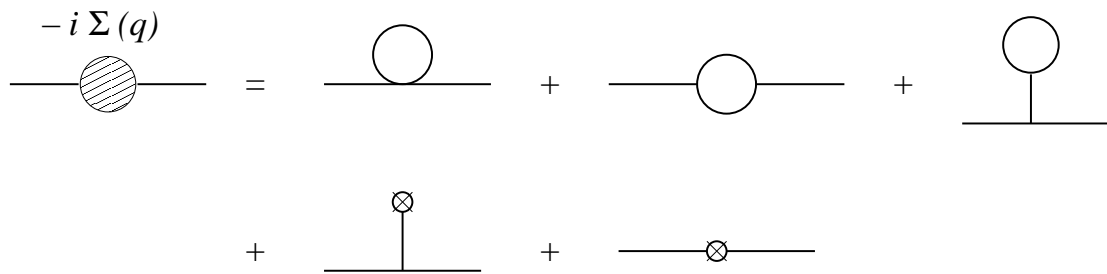


Figure 6.2: The one-loop self energy diagrams.

To determine the renormalization constants, we can impose the on-shell renormalization conditions

$$\Sigma(q^2 = m^2) = 0, \quad \left. \frac{\partial}{\partial q^2} \Sigma(q^2) \right|_{q^2=m^2} = 0 \quad (6.20)$$

This give us the on-shell renormalization constants and $\delta\zeta_v$

$$\delta Z = \frac{9\lambda}{4\pi m} \left(-\frac{1}{3} + \frac{1}{2} \ln \sqrt{3} \right) \quad (6.21)$$

$$\delta\zeta_v = \frac{9\lambda}{4\pi m} \left(\frac{1}{6} + \frac{1}{4} \ln \sqrt{3} \right) \quad (6.22)$$

$$\delta Z_m = \frac{9\lambda}{4\pi m} \left(\frac{2}{3m^2} + \ln \sqrt{3} \right) \quad (6.23)$$

Alternatively, the Z' and m' are defined by the zero momentum renormalization conditions

$$\Sigma(q^2 = 0) = 0, \quad \left. \frac{\partial}{\partial q^2} \Sigma(q^2) \right|_{q^2=0} = 0 \quad (6.24)$$

which give

$$\delta Z' = -\frac{3\lambda}{32\pi m} \quad (6.25)$$

$$\delta\zeta'_v = \frac{21\lambda}{32\pi m} \quad (6.26)$$

$$\delta Z'_m = \frac{39\lambda}{32\pi m} + \frac{3\lambda}{2\pi m^3} \quad (6.27)$$

6.2 One-Loop calculation for $\frac{\langle\phi_0\rangle}{\sqrt{m'}}$

We calculate the vacuum expectation value(VEV) to one-loop order and compare to the simulation results. In the simulation, we measure the bare VEV and $1/Z'$ and m' . In three dimensions, $\langle\phi_0\rangle$ has dimension $\sqrt{\text{mass}}$. Hence, the quantity $\langle\phi_0\rangle/\sqrt{m'}$ is dimensionless and we can look for its continuum limit. In the broken symmetry phase, the VEV will is

$$\langle\phi_0\rangle = V'_0 = \sqrt{Z'}\zeta'_v v', \quad v' = \frac{m'}{\sqrt{2\lambda}} \quad (6.28)$$

So we have

$$\frac{\langle\phi_0\rangle}{\sqrt{m'}} = \sqrt{\frac{m'}{2\lambda}} \left(1 + \frac{1}{2} \delta Z' + \delta\zeta'_v \right) \quad (6.29)$$

$$= \sqrt{\frac{m'}{2\lambda}} \left(1 + \frac{9\lambda}{4\pi m} \frac{13}{48} \right) \quad (6.30)$$

6.3 The calculation for $\frac{1}{Z'}$ to $O(\lambda^2)$

In chapter 3 (and Appendix A), we have derived a bound on the inclusive cross section.

$$\int ds \sigma(s) \leq \frac{1}{Z'} - 1 \quad (6.31)$$

The lattice Monte Carlo simulation provides a nonperturbative result for the right hand side of equation 6.31. To see if this implies any large nonperturbative contribution, we have to compare it to a perturbative case of the equality. (The \mathcal{C} introduced in appendix A is zero in the weak coupling limit.)

$$Z \left(\frac{1}{Z'} - 1 \right) = \int ds \sigma(s) \equiv \mathcal{X} \equiv \sum_N \mathcal{X}^{(N)} \quad (6.32)$$

The index (N) indicates the order of λ^N . So that

$$\frac{1}{Z'} - 1 = \frac{\mathcal{X}}{Z} = \mathcal{X}^{(1)} - \delta Z \mathcal{X}^{(1)} + \mathcal{X}^{(2)} + \dots \quad (6.33)$$

where

$$\mathcal{X}^{(N)} = \sum_n \int ds \sigma_n^{(N)} \quad (6.34)$$

Here we have to sum over all final states with n outgoing particles.

$$\sigma_n(s) = \frac{1}{2\pi s^2} \frac{1}{n!} \int d\Phi_n(s) |\mathcal{G}_{n+1}^c(p_1, \dots, p_n, P)|^2 \quad (6.35)$$

where the phase space integral is

$$\int d\Phi_n = \frac{1}{n!} \int \frac{d^3 p_1}{(2\pi)^3} \delta(p_1^2 - m^2) \dots \int \frac{d^3 p_n}{(2\pi)^3} \delta(p_n^2 - m^2) (2\pi)^3 \delta^3(\vec{P} - \sum p_i) \quad (6.36)$$

The lowest order, $O(\lambda)$, contribution has only one diagram. Figure 6.4 shows the lowest order tree diagrams. So that

$$\begin{aligned} \mathcal{X}^{(1)} &= \int ds \sigma_2^{(1)} \\ &= \int ds \frac{1}{2\pi s^2} \frac{1}{2!} \int d\Phi_2 | -i3\sqrt{2}m\sqrt{\lambda} |^2 \\ &= \frac{9m^2\lambda}{2\pi s^2} \int d\Phi_2 \end{aligned} \quad (6.37)$$

If we choose the CM frame, the two particle phase space integral will be

$$\int d\Phi_2 = \frac{1}{4\sqrt{s}} \quad (6.38)$$

Hence the contribution of order $O(\lambda)$ is

$$\mathcal{X}^{(1)} = \frac{3\lambda}{32\pi m} \quad (6.39)$$

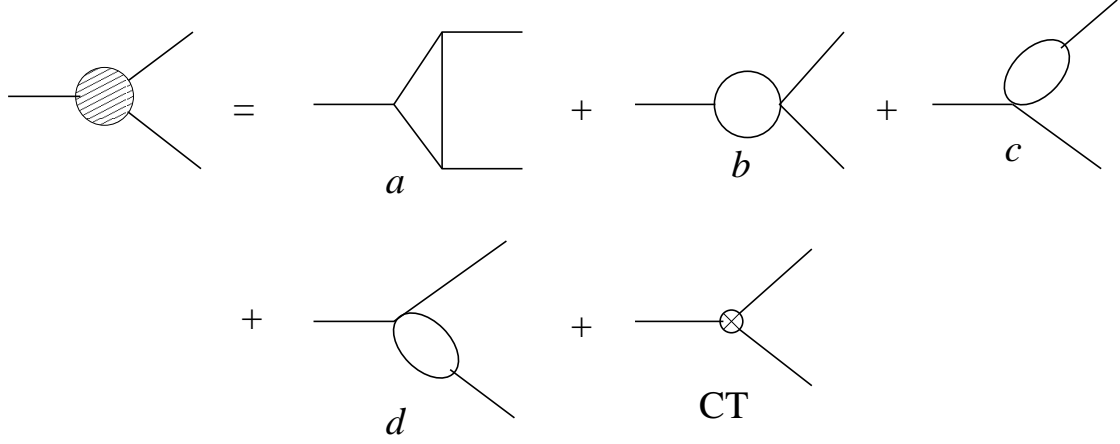


Figure 6.3: The one-loop Feynman diagrams for $n = 2(\mathcal{G}_{\frac{3}{2}}^3)$.

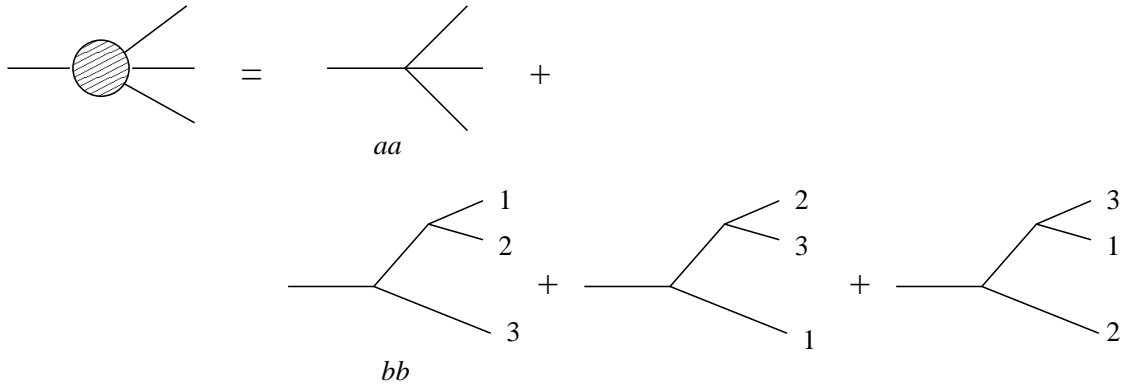


Figure 6.4: The tree diagrams for $n = 3(\mathcal{G}_2^2)$.

By using equation 6.21, the second term in equation 6.33 will be (in order of $O(\lambda^2)$)

$$-\delta Z^{(1)} \mathcal{X}^{(1)} = -\left(\frac{3\lambda}{32\pi m}\right)^2 (-8 + 6 \ln 3) \quad (6.40)$$

The Feynman diagrams and the counter terms for the third term in equation 6.33 are shown in Figure 6.3 and Figure 6.4. Figure 6.3 shows the one-loop Feynman diagram with $n = 2(G - 3mm/\frac{3}{2})$ and Figure 6.4 shows the tree level Feynman diagram for $n = 3(\mathcal{G}_4^{\frac{3}{2}})$. The cross section of order λ^2 is

$$\sigma_2^{(2)}(s) = \frac{1}{2\pi s^2} \frac{1}{2} \int \Phi_2 2\Re[\mathcal{G}_{\frac{1}{2}}^{\frac{1}{2}} \mathcal{G}_{\frac{3}{2}}^{\frac{3}{2}}] \quad (6.41)$$

$$\sigma_3^{(2)}(s) = \frac{1}{2\pi s^2} \frac{1}{3!} \int \Phi_3 2\Re[\mathcal{G}_{\frac{1}{2}}^{\frac{1}{2}} \mathcal{G}_{\frac{3}{2}}^{\frac{3}{2}}] \quad (6.42)$$

We can write

$$\mathcal{X}^{(2)} = \int ds (\sigma_2^{(2)} + \sigma_3^{(2)}) = \mathcal{X}_2^{(2)} + \mathcal{X}_3^{(2)} \quad (6.43)$$

The one-loop Feynman integrals (with $r = \frac{s}{m^2}$) in Figure 6.3 are

$$\begin{aligned} I_a(s) &= i \frac{9\sqrt{2}\lambda^{\frac{3}{2}}}{8\pi} \left(-\frac{6}{2\sqrt{r-3}} \right) \\ &\times \left\{ \frac{x_2}{y_2} \left[\ln \left(\frac{-1-x_2-2y_2}{(-1+x_2)x_2y_2} \right) - \ln \left(\frac{-2+x_2-2y_2}{x_2^2y_2} \right) \right] \right. \\ &\quad \left. - \frac{x_1}{y_1} \left[\ln \left(\frac{-1-x_1-2y_1}{(-1+x_1)x_1y_1} \right) - \ln \left(\frac{-2+x_1-2y_1}{x_1^2y_1} \right) \right] \right\} \end{aligned} \quad (6.44)$$

$$I_b(s) = i \frac{9\sqrt{2}\lambda^{\frac{3}{2}}}{8\pi} \times \frac{2m}{\sqrt{s}} \left[\ln \left(\frac{\sqrt{s}+2m}{\sqrt{s}-2m} \right) \right] \quad (6.45)$$

$$I_c(s) = i \frac{9\sqrt{2}\lambda^{\frac{3}{2}}}{8\pi} \times 2 \ln 3 \quad (6.46)$$

$$I_d(s) = i \frac{9\sqrt{2}\lambda^{\frac{3}{2}}}{8\pi} \times 2 \ln 3 = I_c \quad (6.47)$$

$$\text{C.T.} = i \frac{9\sqrt{2}\lambda^{\frac{3}{2}}}{8\pi} \left[3 - \frac{15}{4} \ln 3 \right] \quad (6.48)$$

where x_1 , x_2 , and y_i are

$$x_1 = \frac{2 + 2\sqrt{r-3}}{4-r} \quad (6.49)$$

$$x_2 = \frac{2 - 2\sqrt{r-3}}{4-r} \quad (6.50)$$

$$y_i = \sqrt{x_i^2 - x_i + 1} \quad (6.51)$$

The two particle phase space integral is the same as before (equation 6.38). Finally, after calculating the s integral, one gets

$$\mathcal{X}_2^{(2)} = \int_{4m^2}^{\infty} ds \sigma_2^{(2)} \quad (6.52)$$

$$= - \left(\frac{3\lambda}{8\pi m} \right)^2 \times 0.496728 \quad (6.53)$$

The Figure 6.4 shows the $n = 3$ case of $O(\lambda^2)$.

$$\mathcal{X}_3^{(2)} = \int ds \sigma_3^{(2)} \quad (6.54)$$

and

$$\sigma_3^{(2)} = \frac{1}{2\pi s^2} \frac{1}{3!} \int d\Phi_3 |\mathcal{G}_4|^2 \quad (6.55)$$

From Figure 6.4, the four point function is

$$\mathcal{G}_4 = T_{aa} + T_{bb} \quad (6.56)$$

the T_{aa} is just the tree diagram in Figure 6.4aa.

$$T_{aa} = -i6\lambda \quad (6.57)$$

The tree level diagram in Figure 6.4bb has six permutations.

$$T_{bb} = -i18m^2\lambda \left[\frac{1}{s_{12} - m^2} + \frac{1}{s_{23} - m^2} + \frac{1}{s_{31} - m^2} \right] \quad (6.58)$$

where

$$s_{ij} = (k_i + k_j)^2 \quad (6.59)$$

is the sum of the momentum of two of the final particles. We make the same simplification that was made on the calculations of the multiplice phase space *ie.* we replace each $k_i \cdot k_j$ by the average $\langle k_i \cdot k_j \rangle$. Then

$$\langle s_{12} - m^2 \rangle = \langle s_{23} - m^2 \rangle = \langle s_{31} - m^2 \rangle = \frac{s}{3} \quad (6.60)$$

Hence, the four point function square can be simplified to

$$|\mathcal{G}_4^2(s)|^2 = 36\lambda^2 \left(1 + 54\frac{m^2}{s} + 729\frac{m^4}{s} \right) \quad (6.61)$$

Since the four point function does no longer depend on the individual momentum of each final particle, the phase space integral becomes easy. We can use the recursion relation 4.17 in chapter four to calculate the space space integral. We find

$$\int d\Phi_3 = \frac{1}{16\pi} \left(1 - \frac{3m}{\sqrt{s}} \right) \quad (6.62)$$

So the contribution from $\mathcal{X}_3^{(2)}$ becomes

$$\mathcal{X}_3^{(2)} = \int ds \frac{1}{2\pi s^2} \frac{1}{6} \int d\phi_3 |\mathcal{G}_4^2(s)|^2 \quad (6.63)$$

$$= \left(\frac{3\lambda}{8\pi m} \right)^2 \times 0.201276 \quad (6.64)$$

Combining equation 6.39,6.40,6.53, and 6.64 gives

$$\frac{1}{Z'} = 1 + \frac{3\lambda}{8\pi m} \times \frac{1}{4} - \left(\frac{3\lambda}{8\pi m} \right)^2 \times 0.206944 \quad (6.65)$$

The mass m in above equation is physical mass under the on-shell scheme. However, we only measure m' from Monte Carlo simulation. In order to compare with

the Monte Carlo results, one should use m' in the perturbation series. The relation between m' and m can be calculated from two point function.

$$G_0(p^2) = Z'G'(p^2) = ZG(p^2), \quad (6.66)$$

and

$$G_0^{-1}(p^2 = 0) = \frac{m'^2}{Z'} = \frac{1}{Z}(m^2 + \Sigma(p^2 = 0)) \quad (6.67)$$

So up to one-loop order, we have

$$\frac{m'^2}{m^2} = \frac{Z'}{Z} \left(1 + \frac{1}{m^2} \Sigma(p^2 = 0)\right) \quad (6.68)$$

$$= 1 + \delta Z' - \delta Z + \frac{1}{m^2} \Sigma(0) \quad (6.69)$$

$$= 1 + \Delta \quad (6.70)$$

From equation 6.70, we have

$$m = m' \left(1 - \frac{\Delta}{2}\right) \quad (6.71)$$

$$\Delta = \frac{9\lambda}{4\pi m} \left(-\frac{13}{24} + \frac{1}{2} \ln 3\right) \quad (6.72)$$

Plug into equation 6.65, we get

$$\frac{1}{Z'} = 1 + \frac{3\lambda}{8\pi m'} \times \frac{1}{4} - \left(\frac{3\lambda}{8\pi m'}\right)^2 \times 0.201214 \quad (6.73)$$

Chapter 7

Analysis and Results

In this chapter, I will discuss the results from the Monte Carlo simulation and compare the results with the perturbation results.

7.1 The Results From the Simulation

The results for the broken symmetry phase are given in Table 7.1. In going down from line to line in the Table 7.1, we have $N \rightarrow 2N$, $\xi_L \rightarrow 2\xi_L$ (approximately). This corresponds to holding the physical lattice size $L = Na$ fixed while halving the physical lattice spacing a . Here we keep the ratio $L/\xi_L \sim 5.6$. This procedure will keep on a line of “constant physics” as approach to the continuum limit (Figure 5.6). Note that the dimensionless quantities λ/m' , $\frac{1}{Z'} - 1$, and $\langle\phi_0\rangle/\sqrt{m'}$ keep the same values, within errors, while we are halving the lattice space. This shows that these values are insensitive to the lattice constant a and approaching to the continuum limit. The Figure 7.1, 7.2, and 7.3 plot the $\frac{\lambda}{m'}$, $\frac{1}{Z'}$ and $\frac{\langle\phi_0\rangle}{\sqrt{m'}}$ in Table 7.1. The plot shows the insensitivity of lattice size for both those quantities. The dashed lines are the fitted lines which show small slopes of the plot. However, it is within the error bar.

Table 7.2, 7.3, and 7.4 shows the finite size effect of the simulation. We have $N \rightarrow 2N$, $\xi_L \rightarrow \xi_L$ (approximately) while the input parameters μ_{0L}^2 , λ_L are held fixed. This corresponds to doubling the physical length of the lattice while keeping the lattice a fixed. This check the sensitivity of the output results to lattice size corrections. The Tables show small discrepancies at smallest lattice size. However, we found that if we keep the ratio $N/\xi_L > 3$, the finite size correction can be ignored. In Table 7.1, we keep the ratio $N/\xi_L \sim 5.6$ so that we can ignore the finite size effect while we are moving along the RG trajectory.

Table 7.1: The results of our simulations on different size lattices(N). The output correlation length $\xi'_L = 1/m'_L$, the dimensionless ratios λ/m' , and $1/Z'$ are given.

μ_{0L}^2	λ_L	N^3	ξ_L	$\frac{\lambda}{m'}$	$\frac{1}{Z'}$	$\frac{\langle\phi_0\rangle}{\sqrt{m'}}$
-0.161	0.2	32^3	5.7(1)	1.13(2)	1.008(2)	0.78(1)
-0.078	0.1	64^3	11.3(4)	1.13(4)	1.012(3)	0.80(2)
-0.0384	0.05	128^3	22.11(1.0)	1.11(5)	1.012(5)	0.80(2)
-0.01905	0.025	256^3	45.4(3.0)	1.13(8)	1.010(8)	0.79(3)

Table 7.2: The finite size effect with fixed input parameters $\mu_{0L}^2 = 0.078$, $\lambda_L = 0.1$.

μ_{0L}^2	λ_L	N^3	ξ_L	$\frac{\lambda}{m'}$	$\frac{1}{Z'}$	$\frac{\langle\phi_0\rangle}{\sqrt{m'}}$
-0.078	0.1	32^3	12.9(4)	1.29(4)	1.0025(10)	0.73(1)
-0.078	0.1	64^3	11.3(4)	1.13(4)	1.012(4)	0.80(2)
-0.078	0.1	128^3	11.2(4)	1.12(4)	1.020(5)	0.80(2)
-0.078	0.1	256^3	10.8(8)	1.08(8)	0.98(2)	0.78(3)

Table 7.3: The finite size effect with fixed input parameters $\mu_{0L}^2 = 0.0384$, $\lambda_L = 0.05$.

μ_{0L}^2	λ_L	N^3	ξ_L	$\frac{\lambda}{m'}$	$\frac{1}{Z'}$	$\frac{\langle\phi_0\rangle}{\sqrt{m'}}$
-0.0384	0.05	32^3	21.1(1.6)	1.06(8)	1.0002(12)	0.71(1)
-0.0384	0.05	64^3	22.1(1.0)	1.10(5)	1.003(2)	0.77(2)
-0.0384	0.05	128^3	22.1(1.0)	1.10(5)	1.012(5)	0.80(2)
-0.0384	0.05	256^3	21.9(1.1)	1.09(6)	1.015(9)	0.79(3)

Table 7.4: The finite size effect with fixed input parameters $\mu_{0L}^2 = 0.01905$, $\lambda_L = 0.025$.

μ_{0L}^2	λ_L	N^3	ξ_L	$\frac{\lambda}{m'}$	$\frac{1}{Z'}$	$\frac{\langle\phi_0\rangle}{\sqrt{m'}}$
-0.01905	0.025	64^3	41.5(6.5)	1.04(16)	1.002(3)	0.78(2)
-0.01905	0.025	128^3	45.1(3.8)	1.127(97)	1.0011(35)	0.77(2)
-0.01905	0.025	256^3	45.4(3.0)	1.13(8)	1.010(8)	0.79(3)

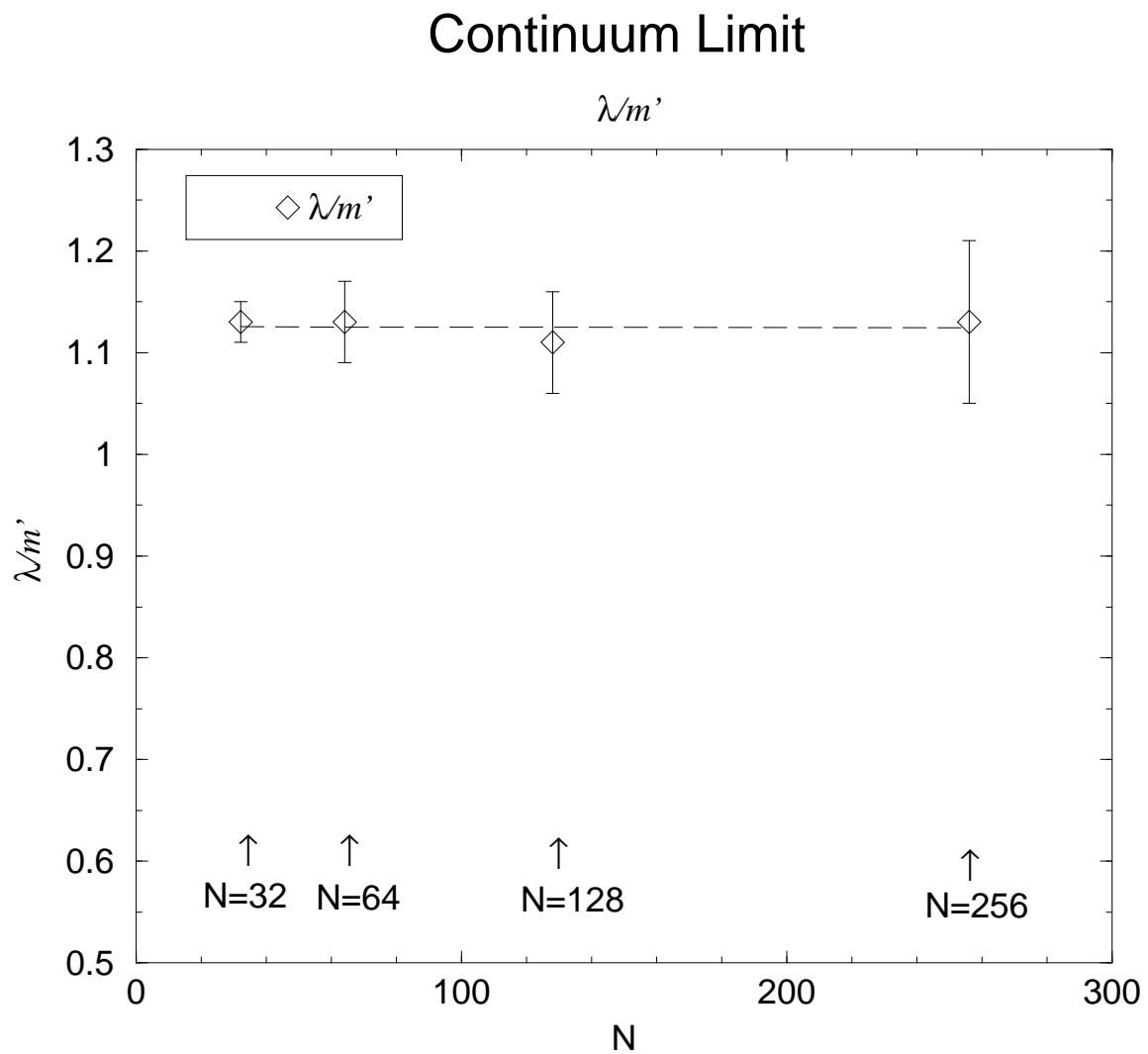


Figure 7.1: Continuum limit for the $\frac{\lambda}{m'}$. The plot shows the insensitivity of lattice size for $\frac{\lambda}{m'}$.

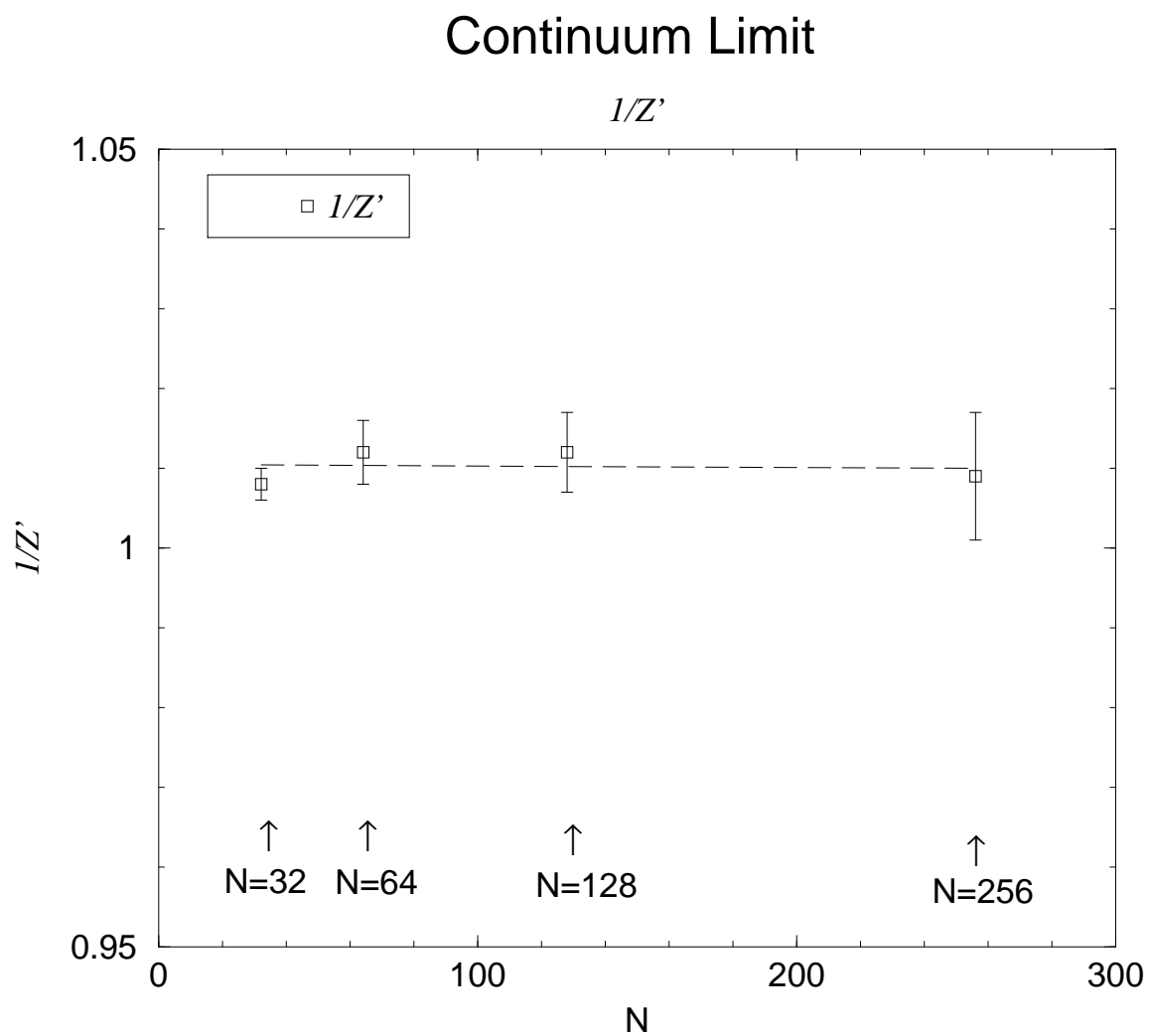


Figure 7.2: Continuum limit for the $\frac{1}{Z'}$. The plot shows the insensitivity of lattice size for $\frac{1}{Z'}$.

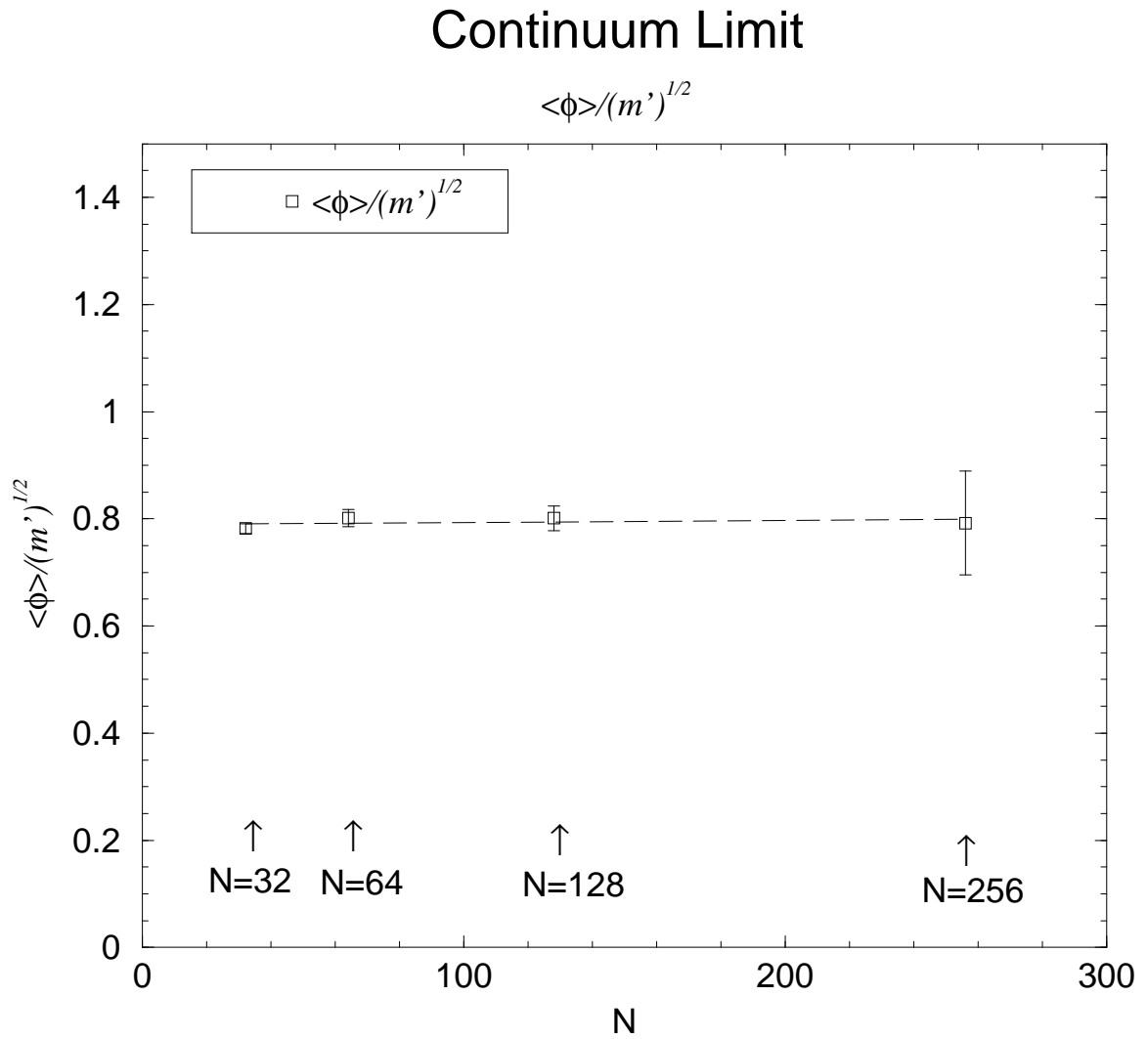


Figure 7.3: Continuum limit for the $\frac{\langle\phi_0\rangle}{\sqrt{m'}}$. The plot shows the insensitivity of lattice size for $\frac{\langle\phi_0\rangle}{\sqrt{m'}}$.

7.2 Discussion and the Conclusion

From Table 7.1, on the 256^3 lattice, we have

$$\xi_L = 45.4 > \frac{74.24 \times m}{\sqrt{3}\lambda} = 37.9, \quad (7.1)$$

This value satisfies condition 3.43. From the table, the $1/Z' - 1$ is

$$\frac{1}{Z'} - 1 = 0.01 \pm 0.008 \quad (7.2)$$

At 95% confidence level, the upper bound of the inclusive cross section is

$$\int ds \sigma(s) \leq 0.026 \quad (7.3)$$

One can see that the numerical result shows no evidence for large multiparticle production at high energy in weakly coupled ϕ_3^4 theory. To gain further insight into the significance of this results, we compare it to the perturbative calculation.

$$\frac{1}{Z'} = 1 + \frac{3\lambda}{8\pi m'} \times \frac{1}{4} - \left(\frac{3\lambda}{8\pi m'} \right)^2 \times 0.201214 \quad (7.4)$$

From Table 7.1, at the $N^3 = 256^3$ lattice, we have $\frac{\lambda}{m'} = 1.13$. So the perturbation result is

$$\frac{1}{Z'} = 1 + 0.1349 \times \frac{1}{4} - (0.1349)^2 \times 0.20121 \quad (7.5)$$

$$= 1 + 0.03372 - 0.00366 \quad (7.6)$$

$$= 1.03006 \quad (7.7)$$

and the $1/Z'$ in Table 7.1 shows

$$\frac{1}{Z'} = 1.010 \pm 0.008 \quad (7.8)$$

we can see that there is little room for multiparticle contributions to the inclusive cross section.

We can also do a perturbative calculation of $\langle \phi_0 \rangle / \sqrt{m'}$ and compare to the lattice Monte Carlo result. The result is striking! The perturbation shows

$$\frac{\langle \phi_0 \rangle}{\sqrt{m'}} = \sqrt{\frac{m'}{2\lambda}} \left(1 + \frac{9\lambda}{4\pi m'} \frac{13}{48} \right) \quad (7.9)$$

For $\frac{\lambda}{m'} = 1.13$, the result is

$$\frac{\langle \phi_0 \rangle}{\sqrt{m'}} = 0.665(1 + 0.219) = 0.811 \quad (7.10)$$

The VEV from our simulation ($N = 256$) is $\langle \phi_0 \rangle = 0.118$ and from Table 7.1, $m' = 0.022$. So the simulation results is

$$\frac{\langle \phi_0 \rangle}{\sqrt{m'}} = 0.795 \pm 0.097 \quad (7.11)$$

In conclusion, our results in equation 7.3 rule out the possibility of large nonperturbative effects coming from high multiplicity production amplitudes in the weakly coupled ϕ_3^4 theory. The comparison with perturbation results from above leaves little room for even small nonperturbative effects.

Appendix A

Multiple zeros case for the function $g^{-1}(z)$

In chapter 3, equation 3.27 leaves open the possibility of zero of $g(z)$ (pole of $g^{-1}(z)$) We deal explicitly with the case of one zero of $g^{-1}(z)$. For the multiple zeros case, one only need to replace the single \mathcal{C} term by $\sum \mathcal{C}_i$. So the equation 3.27 becomes

$$g^{-1}(z) = f(z) + \frac{\mathcal{C}}{z - \xi} + \int_{x_c}^{\infty} dx' \frac{\gamma(x')}{x' - z} \quad (\text{A.1})$$

Figure A.1 shows the possible function of $g(z)$ with one zero. note taht \mathcal{C} is positive.

Because the pole of $g(z)$ is the zero of $g^{-1}(z)$, one can impose the condition $g^{-1}(x_p) = 0$ and $g(z)g^{-1}(z) = 1$ into equation 3.26,A.1 and get

$$g^{-1}(z) = (z - x_p) \left(1 - \frac{\mathcal{C}}{(z - \xi)(\xi - x_p)} + \int_{x_c}^{\infty} dx' \frac{\gamma(x')}{(x' - z)(x' - x_p)} \right) \quad (\text{A.2})$$

In multiparticle production at high energy, $x \gg x_c$, equation A.2 has a pole on the cut and will give us the results the same as equation 3.30 and 3.32.

To calculate the renormalization constant Z , we use $g(z)g^{-1}(z) = 1$ and take the limit $z \rightarrow x_p$ to get

$$\frac{1}{Z} = 1 + \frac{\mathcal{C}}{(\xi - x_p)^2} + \int dx' \frac{\gamma(x')}{(x' - x_p)^2} + \dots \quad (\text{A.3})$$

After analytic continuation to Euclidean space, the inverse two point Green function becomes

$$\frac{1}{G(p)} = (p^2 + m^2) \left[1 + \frac{\mathcal{C}}{(p^2 + \xi^2)(\xi^2 - m^2)} + \int d\kappa^2 \frac{\gamma(\kappa^2)}{(\kappa^2 - m^2)(\kappa^2 + p^2)} \right]. \quad (\text{A.4})$$

Expand in power of p^2

$$\frac{1}{(p^2 + \xi^2)} = \frac{1}{\xi^2} \left(1 - \frac{p^2}{\xi^2} + \frac{p^4}{\xi^4} + \dots \right), \quad (\text{A.5})$$

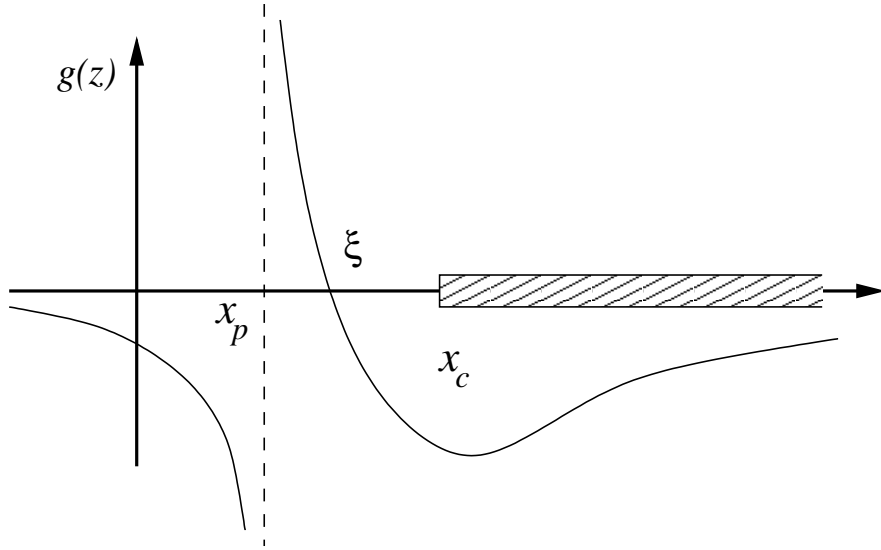


Figure A.1: The function of $g(z)$ with one zero.

we have

$$\begin{aligned}
 G^{-1}(p) &= m^2 \left(1 + \frac{\mathcal{C}}{(\xi^2 - m^2)\xi^2} + \int d\kappa^2 \frac{\gamma(\kappa^2)}{(\kappa^2 - m^2)\kappa^2} \right) \\
 &+ p^2 \left(1 + \frac{\mathcal{C}}{\xi^4} + \int d\kappa^2 \frac{\gamma(\kappa^2)}{\kappa^4} \right) \\
 &+ p^4 \left(-\frac{\mathcal{C}}{\xi^6} \int d\kappa^2 \frac{\gamma(\kappa^2)}{\kappa^6} \right) + \dots
 \end{aligned} \tag{A.6}$$

$$\equiv \frac{1}{Z'} (m'^2 + p^2 + (\dots)p^4 + \dots) \tag{A.7}$$

From equations A.6 and A.7, we have

$$\frac{1}{Z'} = 1 + \frac{\mathcal{C}}{\xi^4} + \int d\kappa^2 \frac{\gamma(\kappa)}{\kappa^4} \tag{A.8}$$

From equations 3.41 and A.8, the upper bound of the integrated inclusive cross section becomes

$$\begin{aligned}
 \int ds \sigma(s) &= Z \int ds \frac{\gamma(s)}{s^2} \\
 &= Z \left(\frac{1}{Z'} - 1 - \frac{\mathcal{C}}{\xi^4} \right)
 \end{aligned} \tag{A.9}$$

$$\leq Z \left(\frac{1}{Z'} - 1 \right) \tag{A.10}$$

$$\leq \left(\frac{1}{Z'} - 1 \right) \tag{A.11}$$

Because the \mathcal{C} is a positive number, the bound remains. It is just a less efficient bound.

Bibliography

- [1] A. Ringwald, Nucl. Phys. **B330**, 1(1990)
- [2] O. Espinosa, Nucl. Phys. **B343**,310(1990)
- [3] J. Zinn-Justin, Phys. Rep. **70**, 109(1981)
- [4] H. Goldberg, Phys. Lett. **B246**, 435(1990)
- [5] J.M. Cornwall, Phys. Lett. **B243**, 271(1990)
- [6] M.B. Voloshin, Phys. Lett. **B293**, 389(1992)
- [7] E.N. Argyres, R.M.P. Kleiss, and C.G. Papadopoulos, Nucl. Phys. **B341**, 42(1993),**B341**, 57(1993)
- [8] R.D. Mawhinney and R.S. Willey, Phys. Rev. Lett. **74**, 3728.(1995)
- [9] L.S. Brown, Phys. Rev. **D46**, R4125(1992)
- [10] J. Glimm and A. Jaffe, *Quantum Physics. A Functional Integral Point of View* (Springer-Verlag, New-York, 1987)
- [11] R. Fernández, Fröhlich and A. Sokal,*Random Walks, Critical Phenomena, and Triviality in Quantum Field Theory* (Springer-Verlag, New York, 1992)
- [12] see Beowulf web site at <http://www.beowulf.org>
- [13] see Top500 supercomputer web site at <http://www.top500.org>
- [14] J. Radajewski and D. Eadline *Beowulf Howto* and *Beowulf Installation and Administration Howto*
- [15] Please refer our web site at <http://www.phyast.pitt.edu/beowulf>
- [16] see Top500 cluster at <http://clusters.top500.org>
- [17] M.B. Voloshin, Minnesota preprint TPI-MINN-92/1-T
- [18] N.I. Fuss, Nova Acta Academia Scientiarum Petropolitana **9** (1791) 445.
- [19] F. Lurcat and P. Mazur, *Nuovo Cimento* **XXXI**, no.1(1964) 140.

- [20] E. Fermi, *Progr. Theoret. Phys.*, **5**, 570(1950). see also R. Hagedorn *Relativistic Kinematics*,(Benjamin Inc, Massachusetts, 1973)
- [21] I. Montvay and G. Munster, *Quantum Fields on a Lattice* (Cambridge, United Kingdom 1994), or M.E.J. Newman and G.T. Barkema, *Monte Carlo Methods in Statistical Physics*(Oxford, New York 1999).
- [22] R. Swendsen and J.S. Wang, *Phys. Rev. Lett.* **58**, 86(1987)
- [23] C.M. Fortuin and P.W. Kasteleyn, *Physica* (Amsterdam) **57**, 536(1972).
- [24] U. Wolff, *Phys. Rev. Lett.* **23**, 361(1989)
- [25] D. Kandel, E. Domany, D. Ron, A. Brandt and E. Loh, Jr., *Phys. Rev. Lett.* **60**,1591(1988).
- [26] R.C. Brower and P. Tamayo, *Phys. Rev. Lett.* **62** 1087(1989)
- [27] P.C. Hoenberg and B. Halperin, *Rev. Mod. Phys* **49**, 435 (1977).
- [28] The values are taken from Coddington and Bailie(1992), Matz *et al.*(1994) and Nightingale and Blote(1996). The dynamic exponent of Metropolis algorithm has not been measured in four dimensions.
- [29] M. Tsypin, *Phys. Rev. Lett.* **73**, 2015(1994); or M. Tsypin e-print hep-lat/9401034.
- [30] J. Rudnick, W. Lay, and D. Jasnow, *Phys Rev* **E58**, 2902(1998)